Effects of microscopic boundary conditions on the deformation behavior of small-volume metallic glasses

P. Thamburaja, J. Liu

PII: S0020-7683(14)00358-8
DOI: http://dx.doi.org/10.1016/j.ijsolstr.2014.09.011
Reference: SAS 8507

To appear in: *International Journal of Solids and Structures*

Received Date: 13 February 2014
Revised Date: 12 September 2014
Accepted Date: 15 September 2014

Please cite this article as: Thamburaja, P., Liu, J., Effects of microscopic boundary conditions on the deformation behavior of small-volume metallic glasses, *International Journal of Solids and Structures* (2014), doi: http://dx.doi.org/10.1016/j.ijsolstr.2014.09.011

Effects of microscopic boundary conditions on the deformation behavior of small-volume metallic glasses*

P Thamburaja[a,*], J Liu[b]

[a]*Department of Mechanical and Materials Engineering, National University of Malaysia (UKM), Bangi 43600, Malaysia*
[b]*Department of Mechanical Engineering, National University of Singapore (NUS), Singapore 117576*

Abstract

Although large-volume metallic glasses (MG) are susceptible to shear localization due to their intrinsically strain-softening response, recent experiments and molecular dynamics simulations have shown that small-volume MGs samples are able to exhibit work hardening response. Here, we seek to address two issues regarding the mechanical response of small-volume MGs at low homologous temperatures from a continuum-based modeling perspective: (1) are MGs capable of exhibiting a work hardening response, and (2) what is the physical mechanism which causes its work hardening response?

Along with implementing a recently-developed finite-deformation, strain gradient plasticity-based constitutive model for MGs into a self-developed finite-element code, we study the tensile response of small-volume MG samples of various sizes through finite-element simulations. Our simulations show that small-volume MG samples are capable of exhibiting a work hardening response provided the following conditions are met: (a) the sample size is small enough, and (b) the appropriate microscopic boundary conditions for the free volume are imposed on the sample.

Keywords: Amorphous metals, Constitutive model, Strain gradient plasticity, Finite-elements, Microscopic boundary conditions

*Corresponding author. Email: prakash.thamburaja@gmail.com

*This paper is dedicated to Prof. Lallit Anand (MIT) on the occasion of him receiving the 2014 Daniel C. Drucker Medal.

1. Introduction

Metallic glasses (or amorphous metals) are structureless materials which are void of point defects and line defects (dislocations) that weaken conventional crystalline metals. Some of the recent major applications involving the use of amorphous metals are in the area of micro & nano-technology, precision tools and medical implants (Guo et al., 2007; Kumar et al., 2011; Chen, 2011). This has resulted in a surge of experimental activity in the area of mechanical characterization of small-volume amorphous metals (Guo et al., 2007; Volkert et al., 2008; Dubach et al., 2009; Bharathula et al., 2010; Jang and Greer, 2010; Jang et al., 2011; Tian et al., 2012; Wang et al., 2012).

Although amorphous metals are generally very much stronger compared to conventional crystalline metals, they have limited macroscopic ductility due its propensity for shear band formation and its catastrophic propagation. This phenomenon is observed in amorphous metals since they are intrinsically *strain-softening* materials as a result of stress (or plastic deformation)-induced free volume creation (Spaepen, 1977; Argon, 1979; Schuh et al., 2007). Therefore, the practical use of amorphous metals as key engineering materials can be further popularized if they are able to possess work hardening (or strain-hardening) characteristics which are desirable in avoiding catastrophic shear localization.

Recent room-temperature monotonic and cyclic tensile experiments conducted by Jang and Greer (2010) and Tian et al. (2012) on *small-volume* (or nano-sized) monolithic amorphous metal samples have shown that amorphous metals have the ability to exhibit a post-yield work hardening stress-strain response cf. Figures 1a and 1b, respectively. In our opinion, this is a remarkable discovery for the following reasons: (a) dislocations are not present in amorphous metals, and (b) the generation of multiple shear bands and their interactions as a mechanism for the observed post-yield work hardening response in *bulk* amorphous metals (Schroers and Johnson, 2004; Das et al., 2005) are not realizable in small-volume amorphous metals due to their limited volume (Guo et al., 2007; Jang and Greer, 2010).

The post-yield work hardening stress-strain response has also been observed in the room-temperature molecular dynamics simulations of Li and Li (2006) and Pang et al. (2010) cf. Figures 1c and 1d, respectively[2]. The

[2]Although the applied strain-rates in the molecular dynamics simulations are orders of magnitude higher than that encountered in physical experiments, the qualitative stress-

numerically-simulated tensile stress-strain curves shown in Figure 1 were obtained from the molecular dynamics simulations of sufficiently relaxed, nano-sized binary-based amorphous metal systems. Since the sample sizes modeled in these aforementioned simulations were in the order of the shear band nucleus, no shear bands were formed in the samples during deformation (Li and Li, 2006; Pang et al., 2010), and the work hardening behavior in the stress-strain responses shown in Li and Li (2006) and Pang et al. (2010) is not caused by the formation & interaction of shear bands. Furthermore, deformation-induced nanocrystallization has also been ruled out as a cause for large plastic deformation and work hardening behavior (Guo et al., 2007; Pang et al., 2010). Therefore, based on the experiments and molecular dynamics simulations shown in Figure 1, we concur with the analysis of Pang et al. (2010) that the physical mechanism responsible for the work hardening response in small-volume amorphous metals is still not fully understood[3].

To investigate the sample size effects on the deformation behavior of amorphous metals from a continuum perspective, we require the usage of non-local-based theories. Recently, Thamburaja (2011) developed a finite-deformation, gradient-plasticity-based constitutive model which was implemented into a commercially available finite-element program. Through finite-element simulations, they have shown that amorphous metals are capable of exhibiting the transition from catastrophic shear localization to stable shear localization to homogeneous deformation behavior with decreasing sample volume. As the sample volume becomes small, it is known that its deformation behavior becomes very sensitive to the types of imposed boundary conditions for the microstructural variables i.e. *microscopic boundary conditions* e.g. see the work of Bittencourt et al. (2003) on crystalline metals. However, Thamburaja (2011) did not investigate the effects of different types of microscopic boundary conditions on the deformation behavior of small-volume amorphous metal samples.

Therefore, the main purposes of this work are to: (a) implement the finite-deformation, gradient-plasticity-based constitutive model of Thamburaja (2011) into a self-developed finite-element framework where each node of each element has the free volume (the microstructural variable for amor-

strain trends observed in both methods are similar.

[3]Tian et al. (2012) have *speculated* that the work hardening in small-volume amorphous metals is caused by the delayed shear band nucleation due to the small sample size.

phous metals) and three independent displacements as degrees of freedom; (b) investigate the effect of different types microscopic boundary conditions on the deformation behavior of small-volume amorphous metals via finite-element simulations; and (c) ascertain the physical causes for the observed work hardening behavior in small-volume amorphous metals.

The structure of this paper is as follows: in Section 2, we summarize the key equations of the finite-deformation, gradient-plasticity-based constitutive model for amorphous metals developed by Thamburaja (2011). In Section 3, we briefly describe the novel computational aspects of our finite-element implementation of the constitutive model of Thamburaja (2011). We also provide the key steps of the time-integration procedure used to implement the constitutive model in this section. In Section 4, we perform monotonic and cyclic tension finite-element simulations on small-volume amorphous metal samples to investigate the causes for the work hardening response observed in these traditionally strain-softening materials. Finally, we present our conclusion in Section 5[4] .

2. Constitutive model

In this section, we summarize the finite-deformation, gradient plasticity-based constitutive model for amorphous metals developed by Thamburaja (2011). This constitutive theory was derived under isothermal conditions and in the absence of heat fluxes/sources. For more information regarding the development of the constitutive model, please refer to Thamburaja (2011).

Notation: Second-order tensors are denoted by bold upper-case Roman alphabets e.g. $\mathbf{A}$, $\mathbf{A}^*$, $\mathbf{H}$ etc. The divergence, gradient and Laplacian operators with respect to *referential* coordinates are denoted by Div, ∇ and ∇^2, respectively. The second-order identity tensor is denoted by $\mathbf{I}$. The transpose of tensor $\mathbf{A}$ is written as $\mathbf{A}^\top$. The inverse of tensors $\mathbf{A}$ and $\mathbf{A}^\top$ are respectively written as $\mathbf{A}^{-1}$ and $\mathbf{A}^{-\top}$. The determinant of tensor $\mathbf{A}$ is denoted by $\det \mathbf{A}$. The product between two tensors $\mathbf{A}$ and $\mathbf{H}$ is denoted by $\mathbf{AH}$. The scalar product between two vectors $\mathbf{a}$ and $\mathbf{b}$ is denoted by $\mathbf{a} \cdot \mathbf{b}$. The scalar product between two tensors $\mathbf{A}$ and $\mathbf{H}$ is denoted by $\mathbf{A} : \mathbf{H}$. The

[4]For some of our recent work on the modeling of metallic glass behavior at high homologous temperatures, see Ekambaram et al. (2008, 2010). Furthermore, please refer to Bargmann et al. (2014) for recent efforts in modeling the response of submicron-sized metallic glasses.

symmetric part of tensor $\mathbf{A}$ is denoted by $\operatorname{sym}\mathbf{A} \equiv (1/2)\,(\mathbf{A}+\mathbf{A}^{\top})$. The trace of tensor $\mathbf{A}$ is denoted by $\operatorname{trace}\mathbf{A} \equiv \mathbf{I}:\mathbf{A}$. The deviatoric part of tensor $\mathbf{A}$ is denoted by $\operatorname{dev}\mathbf{A} \equiv \mathbf{A} - (1/3)\,(\operatorname{trace}\mathbf{A})\,\mathbf{I}$. The l^2-norm of vector $\mathbf{a}$ is denoted by $|\mathbf{a}| \equiv \sqrt{\mathbf{a}\cdot\mathbf{a}} \geq 0$. The Frobenius norm of tensor $\mathbf{A}$ is denoted by $\|\mathbf{A}\| \equiv \sqrt{\mathbf{A}:\mathbf{A}}$.

The governing variables in the constitutive theory are (a) the Helmholtz free energy per unit *reference* volume, ψ; (b) the total deformation gradient, $\mathbf{F}$ with $\mathrm{J} = \det\mathbf{F} > 0$; (c) the Cauchy stress, $\mathbf{T} = \mathbf{T}^{\top}$; (d) the plastic distortion, $\mathbf{F}^p$ with $\mathrm{J}^p = \det\mathbf{F}^p > 0$. It describes the cumulative deformation due to plastic shearing and free volume generation; (e) the elastic distortion, $\mathbf{F}^e = \mathbf{F}\mathbf{F}^{p-1}$ with $\mathrm{J}^e = \det\mathbf{F}^e > 0$. It describes the elastic deformation of the interatomic structure. The elastic distortion is further decomposed into $\mathbf{F}^e = \mathbf{R}^e\mathbf{U}^e$ where $\mathbf{R}^e$ denotes the elastic rotation and $\mathbf{U}^e$ the elastic stretch. The tensors $\mathbf{R}^e$ and $\mathbf{U}^e$ have the properties $\mathbf{R}^e = \mathbf{R}^{e-\top}$, $\det\mathbf{R}^e = 1$, $\mathbf{U}^e = \mathbf{U}^{e\top}$ and $\det\mathbf{U}^e > 0$; (f) the elastic right Cauchy-Green strain, $\mathbf{C}^e = \mathbf{F}^{e\top}\mathbf{F}^e = \mathbf{U}^{e2}$; (g) the elastic Hencky strain, $\mathbf{E}^e = (1/2)\ln\mathbf{C}^e = \ln\mathbf{U}^e$; (h) the elastic stress, $\mathbf{T}^e = \mathrm{J}\mathbf{R}^{e\top}\mathbf{T}\mathbf{R}^e$; (i) the plastic shear strain, $\gamma \geq 0$; and (j) the free volume, $\xi \geq 0$. It represents a measure of the *defect* density in amorphous metals.

• *Free energy*

The Helmholtz free energy density, ψ is given by

$$\psi = \hat{\psi}(\mathbf{E}^e, \nabla\xi, \xi) = \psi^e + \psi^g + \psi^{\xi}.$$

The elastic free energy density, $\psi^e = \hat{\psi}^e(\mathbf{E}^e)$ is given by the classical relation

$$\psi^e = \mu\,\|\operatorname{dev}\mathbf{E}^e\|^2 + (1/2)\,\kappa\,(\operatorname{trace}\mathbf{E}^e)^2$$

where the constants $\mu > 0$ and $\kappa > 0$ denote the shear and bulk moduli, respectively. The quantity $\psi^g = \hat{\psi}^g(\nabla\xi)$ represents the gradient free energy density, and it is taken as

$$\psi^g = (1/2)\,s_{\xi 1}|\nabla\xi|^2$$

where the constant $s_{\xi 1} \geq 0$ represents the gradient energy coefficient (units of energy per unit length). The gradient energy penalizes the formation of shear bands and introduces a material *length scale* into the constitutive model. Finally, the defect free energy density, $\psi^{\xi} = \hat{\psi}^{\xi}(\xi)$ is given by

$$\psi^{\xi} = (1/2)s_{\xi 2}\xi^2 - s_{\xi 2}\xi\xi_T$$

where the constant $s_{\xi 2} \geq 0$ represents the defect energy coefficient (units of energy per unit volume) and the constant $\xi_T > 0$ represents the *fully-annealed* value for the free volume.

• *Constitutive equation for elastic stress*

The constitutive equation for the elastic stress is given by

$$\mathbf{T}^e = 2\mathbf{U}^e \, \frac{\partial \psi}{\partial \mathbf{C}^e} \, \mathbf{U}^e = 2\mu \, (\operatorname{dev} \mathbf{E}^e) + \kappa \, (\operatorname{trace} \mathbf{E}^e) \, \mathbf{I}.$$

• *Flow rule*

The flow rule provides an evolution equation for the plastic distortion $\mathbf{F}^p$, and it is taken as

$$\dot{\mathbf{F}}^p = \mathbf{D}^p \mathbf{F}^p,$$

$$\mathbf{D}^p = \dot{\gamma} \sqrt{\frac{1}{2}} \, \mathbf{N}^p \, + \, \dot{\xi} \left(\frac{1}{3} \right) \mathbf{I}, \quad \mathbf{N}^p = \frac{\operatorname{dev} \mathbf{T}^e}{\| \operatorname{dev} \mathbf{T}^e \|}.$$

The tensors $\mathbf{D}^p$ and $\mathbf{N}^p$ respectively denote the rate of plastic stretching and the direction for plastic flow. The scalar variables $\dot{\gamma} \geq 0$ and $\dot{\xi}$ represent the *plastic shearing rate* and the *free volume generation rate*, respectively. The rate of free volume generation and plastic shearing rate are coupled by the relation $\dot{\xi} = \zeta \dot{\gamma} + \dot{\xi}^*$ where the dimensionless material constant $\zeta \geq 0$ denotes the free volume creation parameter, and the quantity $\dot{\xi}^*$ represents mechanisms for free volume generation *other* than plastic shearing (more on this later).

• *Evolution equation for the plastic shear strain*

The constitutive relation for the plastic shearing rate is

$$\dot{\gamma} = \dot{\gamma}_o \left(\frac{< f^p >}{c} \right)^{1/a},$$

$$f^p = \bar{\sigma} \, - \, \bar{\sigma}_{int} \, - \, \zeta [s_{\xi 2} (\xi - \xi_T) + \bar{p} \,].$$

The scalar variable f^p denotes the driving force for *plastic shearing* with variables $\bar{\sigma} = \sqrt{1/2} \, \| \operatorname{dev} \mathbf{T}^e \| \geq 0$ and $\bar{p} = -(1/3) \operatorname{trace} \mathbf{T}^e$ being the *equivalent shear stress* and the *hydrostatic pressure*, respectively. With the vectors $\mathbf{m} = \nabla \xi$ and $\mathbf{h} = \dfrac{\partial \psi}{\partial \mathbf{m}}$, the quantity $\bar{\sigma}_{int} = -\zeta \operatorname{Div} \mathbf{h} = -\zeta s_{\xi 1} (\nabla^2 \xi)$ denotes

the long-range interaction stress between defects[5]. The material parameter $c = \hat{c}(\xi) > 0$ represents the *intrinsic resistance* to plastic shearing i.e. the *cohesion* of the material (units of stress). Finally, the material constants $\dot{\gamma}_o > 0$ and $a > 0$ respectively denote the reference shearing rate and the rate-sensitivity parameter.

• *Evolution equation for the free volume*

The rate of free volume generation is given by

$$\dot{\xi} = K\left(\nabla^2\xi\right) + \zeta\dot{\gamma} - \left(\frac{\nu_*\bar{p}}{s_{\xi 3}}\right) - \left(\frac{\nu_* s_{\xi 2}}{s_{\xi 3}}\right)(\xi - \xi_T). \tag{1}$$

With regards to the terms on the right-hand side of equation (1), the first term is the diffusion of free volume with parameter $K = \nu_*(s_{\xi 1}/s_{\xi 3})$ representing the free volume diffusion coefficient, the second term is the plastic shearing-induced free volume generation, the third term is the generation of free volume caused by the effect of hydrostatic pressure, and the fourth term is the annihilation of free volume due to structural relaxation. From equation (1), we can clearly see that

$$\dot{\xi}^* = K\left(\nabla^2\xi\right) - \left(\frac{\nu_*\bar{p}}{s_{\xi 3}}\right) - \left(\frac{\nu_* s_{\xi 2}}{s_{\xi 3}}\right)(\xi - \xi_T)$$

since $\dot{\xi} = \zeta\dot{\gamma} + \dot{\xi}^*$. The material constant $s_{\xi 3} > 0$ represents the resistance to free volume generation due to mechanisms other than plastic shearing (units of energy per unit volume), and $\nu_* = \hat{\nu}_*(\xi)$ represents a frequency-like term (units of time inverse). From Thamburaja (2011), we have $\nu_* = \nu_o\sqrt{\exp(-\varphi/\xi)}$ where the material parameter $\nu_o > 0$ represents a constant reference frequency (units of time inverse) with the dimensionless geometric constant $\varphi > 0$.

• *Evolution law for the cohesion*

The evolution law for the the cohesion is taken as

$$\dot{c} = q\,c\,\dot{\xi} \implies c = c_o\exp\left\{q\left(\xi - \xi_o\right)\right\}$$

[5]The definition for the long-range interaction stress between defects adopted in this work differs slightly from the definition used in Thamburaja (2011).

where $c_o > 0$ and $\xi_o > 0$ represents the *initial* values for the cohesion and free volume, respectively, and the dimensionless constant $q < 0$ ensures that the cohesion *decreases* when free volume is created i.e. when $\dot{\xi} > 0$.

3. Computational procedure

We have implemented the constitutive model described in Section 2 into a self-developed finite-element code using an explicit[6] finite-element formulation. In this Section, we will briefly describe the main aspects of our explicit finite-element algorithm.

3.1. Finite-element discretization of the free volume evolution equation

Consider a body which occupies a region $\mathcal{R}$ in the *reference* configuration with $\mathbf{n}$ denoting the outward unit normal vector on the boundary surface $\mathcal{S}$ of $\mathcal{R}$. Let dA and dV denote the area element and volume element, respectively, in the *reference* configuration. The *microscopic* boundary conditions imposed on the body are

$$\nabla\xi \cdot \mathbf{n} = 0 \ \text{ on } \ \mathcal{S}^n, \quad \dot{\xi} = 0 \ \text{ on } \ \mathcal{S}^d \tag{2}$$

where the boundary surfaces $\mathcal{S}^n \subseteq \mathcal{S}$ and $\mathcal{S}^d \subseteq \mathcal{S}$ with $\mathcal{S}^n \cap \mathcal{S}^d = \varnothing$ and $\mathcal{S}^n \cup \mathcal{S}^d = \mathcal{S}$. Equation $(2)_1$ represents a *natural* (or Neumann-type) boundary condition, and equation $(2)_2$ represents an *essential* (or Dirichlet-type) boundary condition. In strain-gradient plasticity terminology e.g. Gurtin (2002), equation $(2)_1$ resembles a *microscopically free* boundary condition, and equation $(2)_2$ resembles a *microscopically hard* boundary condition.

In our finite-element formulation, the displacement and free volume are treated as nodal degrees of freedom, and the standard Galerkin weak form method is used to discretize the free volume evolution equation

$$\dot{\xi} = K\left(\nabla^2\xi\right) + f^{\xi} \tag{3}$$

[6]As metallic glasses are susceptible to (catastrophic) shear banding, we have chosen to numerically implement the constitutive model presented in Section 2 into an explicit finite-element formulation since explicit approaches exhibit an advantage over the implicit approaches when it comes to the ease of treating material instabilities. Furthermore, the presently developed numerical tool can be used to aid our future studies on impact & dynamic fracture of BMGs, and also contact-dominated simulations of small-volume amorphous metals where frictional effects become very important. Recently, explicit-based finite-element algorithms are also finding increased use in strain gradient plasticity-type modeling work cf. Lee and Han (2010, 2012) and Bittencourt (2014).

where for convenience, we have written

$$f^{\xi} = \zeta\dot{\gamma} \; - \; \left(\frac{\nu_* \bar{p}}{s_{\xi 3}}\right) \; - \; \left(\frac{\nu_* s_{\xi 2}}{s_{\xi 3}}\right)(\xi - \xi_T).$$

Using the variation of the free volume $\delta\xi$ as a trial function, we can write equation (3) in the *variational form*

$$\int_{\mathcal{R}} (\dot{\xi})\, \delta\xi \, \mathrm{dV} = \int_{\mathcal{R}} (K\nabla^2\xi \; + \; f^{\xi})\, \delta\xi \, \mathrm{dV}. \tag{4}$$

From the boundary condition given by equation $(2)_2$, we have

$$\delta\xi = 0 \;\; \text{on} \;\; \mathcal{S}^d. \tag{5}$$

It is important to note that $\delta\xi$ is arbitrary except on $\mathcal{S}^d$.

The application of the integration by parts technique on equation (4) results in

$$\begin{aligned} &\int_{\mathcal{R}} (\dot{\xi})\, \delta\xi \, dV = \int_{\mathcal{S}} \{K(\nabla\xi \cdot \mathbf{n})\}\, \delta\xi \, \mathrm{dA} - \\ &\int_{\mathcal{R}} K(\nabla(\delta\xi) \cdot \nabla\xi) \, \mathrm{dV} - \int_{\mathcal{R}} (\nabla K \cdot \nabla\xi)\, \delta\xi \, \mathrm{dV} + \\ &\int_{\mathcal{R}} (f^{\xi})\, \delta\xi \, \mathrm{dV}. \end{aligned} \tag{6}$$

Since $K = \nu_*(s_{\xi 1}/s_{\xi 3}) = \nu_o \sqrt{\exp(-\varphi/\xi)}\,(s_{\xi 1}/s_{\xi 3})$, we have

$$\nabla K = \bar{K}\nabla\xi \tag{7}$$

where the quantity $\bar{K} = (1/2)(\varphi/\xi^2)K$. Using equations $(2)_1$ and (5), we can see that the first term on the right-hand side of equation (6)

$$\int_{\mathcal{S}} \{K(\nabla\xi \cdot \mathbf{n})\}\, \delta\xi \, \mathrm{dA} = \int_{\mathcal{S}^n} \{K(\nabla\xi \cdot \mathbf{n})\}\, \delta\xi \, \mathrm{dA} + \int_{\mathcal{S}^d} \{K(\nabla\xi \cdot \mathbf{n})\}\, \delta\xi \, \mathrm{dA} = 0,$$

and hence equation (6) is then reduced to

$$\int_{\mathcal{R}} (\dot{\xi})\, \delta\xi \, dV = \int_{\mathcal{R}} (f^{\xi} - \nabla K \cdot \nabla\xi)\, \delta\xi \; - \; K(\nabla(\delta\xi) \cdot \nabla\xi) \, \mathrm{dV}. \tag{8}$$

The body $\mathcal{R}$ is then discretized into n_{el} elements i.e. $\mathcal{R} = \bigcup_{m=1}^{n_{el}} \mathcal{R}_m$ where $\mathcal{R}_m$ represents the domain occupied by element m in the *reference* configuration with integers $m = 1, 2, \ldots, n_{el}$. Let vector $\mathbf{x} \equiv (x_1, x_2, x_3)$ denote the *reference* position of an arbitrary material point in $\mathcal{R}$. We label the nodes of each element by integers $i = 1, 2, \ldots, n_n$ where n_n is the total number of nodes for each element, and the shape function associated with node i of each element by $N_i = \hat{N}_i(\mathbf{x})$. The free volume and rate of free volume generation at any point within an element are determined by the respective relations

$$\xi = \sum_{i=1}^{n_n} N_i \xi_i \quad \text{and} \quad \dot{\xi} = \sum_{i=1}^{n_n} N_i \dot{\xi}_i \tag{9}$$

where ξ_i is the free volume at node i of the element, and $\dot{\xi}_i$ is the rate of free volume generation at node i of the element. We also have

$$\delta\xi = \sum_{i=1}^{n_n} N_i \delta\xi_i \tag{10}$$

where $\delta\xi_i$ is the variation of the free volume at node i of an element. From equations (5) and (10), we can see that $\delta\xi_i = 0$ if node i of the element is located on $\mathcal{S}^d$. Furthermore, it is also important to note that $\delta\xi_i$ is arbitrary except if node i of the element is located on $\mathcal{S}^d$.

Finally, we substitute equation (7) and the element level relations given by equations $(9)_{1,2}$ and (10) into equation (8), and employ standard techniques used in finite-element analysis to obtain the global level finite-element relation

$$\mathbf{M}^{\xi}\dot{\mathbf{v}}^{\xi} = -\mathbf{K}^{\xi}\mathbf{v}^{\xi} + \mathbf{f}^{\xi} \tag{11}$$

where $\mathbf{M}^{\xi} = \mathop{\mathbb{A}}_{m=1}^{n_{el}} \mathbf{M}^{\xi}_m$ is the *global* level free volume mass-like matrix with $\mathbf{M}^{\xi}_m = \int_{\mathcal{R}_m} \mathbf{N}^{\top}\mathbf{N}\,\mathrm{dV}$ being the *element* level free volume mass-like matrix of element m, $\mathbf{K}^{\xi} = \mathop{\mathbb{A}}_{m=1}^{n_{el}} \mathbf{K}^{\xi}_m$ is the *global* level free volume stiffness-like matrix with

$$\mathbf{K}^{\xi}_m = \int_{\mathcal{R}_m} \mathbf{B}^{\top} K \mathbf{B} + \mathbf{N}^{\top}\left(\bar{K}\nabla\xi\right)\mathbf{B}\,\mathrm{dV} \tag{12}$$

being the *element* level free volume stiffness-like matrix of element m, and

$\mathbf{f}^{\xi} = \mathop{\mathbb{A}}_{m=1}^{n_{el}} \mathbf{f}_m^{\xi}$ is the *global* level free volume force-like vector with

$$\mathbf{f}_m^{\xi} = \int_{\mathcal{R}_m} \mathbf{N}^{\top} f^{\xi} \, \mathrm{dV} \tag{13}$$

being the *element* level free volume force-like vector of element m. The global level vectors $\mathbf{v}^{\xi}$ and $\dot{\mathbf{v}}^{\xi}$ contain the body's nodal free volumes and free volume generation rates, respectively, and $\mathbb{A}$ is the finite-element assembly operator cf. Belytschko et al. (2000). The element level matrices $\mathbf{N}$ and $\mathbf{B}$ are respectively given as

$$\mathbf{N} = \begin{bmatrix} N_1 & N_2 & \cdots & N_{n_n} \end{bmatrix},$$

$$\mathbf{B} = \begin{bmatrix} \dfrac{\partial N_1}{\partial x_1} & \dfrac{\partial N_2}{\partial x_1} & \cdots & \dfrac{\partial N_{n_n}}{\partial x_1} \\ \dfrac{\partial N_1}{\partial x_2} & \dfrac{\partial N_2}{\partial x_2} & \cdots & \dfrac{\partial N_{n_n}}{\partial x_2} \\ \dfrac{\partial N_1}{\partial x_3} & \dfrac{\partial N_2}{\partial x_3} & \cdots & \dfrac{\partial N_{n_n}}{\partial x_3} \end{bmatrix}.$$

Equation (11) is then used to calculate the rate of free volume generation at the nodes of the body.

3.2. Calculation of the gradient and Laplacian of the free volume at the Gauss points

We label the Gauss points for each element by integers $j = 1, 2, \ldots, n_g$ where n_g denotes the total number of Gauss points for each element. In the present work, we have used continuum three-dimensional hexahedral elements for our finite-element simulations where each element has eight nodes and eight Gauss points i.e. $n_n = 8$ and $n_g = 8$. In this subsection, let $\{\#\}_m$ represent a quantity $\#$ of element m where integers $m = 1, 2, \ldots, n_{el}$.

Following a similar methodology proposed by Park et al. (2012), we calculate the Laplacian of the free volume at each Gauss point of each element by the following steps:

DO $m = 1, n_{el}$ (**Begin loop over the elements**)

Step 1. Evaluate the first-order derivative of the free volume with respect to material coordinate x_k at Gauss point j of element m, $\left\{\left(\frac{\partial \xi}{\partial x_k}\right)^g_j\right\}_m$:

$$\left\{\left(\frac{\partial \xi}{\partial x_k}\right)^g_j\right\}_m = \sum_{i=1}^{n_n}\left(\frac{\partial N_i}{\partial x_k}\right)_j \{\xi_i\}_m, \quad j=1,2,\ldots,n_g, \quad k=1,2,3.$$

The quantity $\left(\frac{\partial N_i}{\partial x_k}\right)_j$ denotes the value of the first-order derivative of the element level shape function associated with node i with respect to material coordinate x_k at Gauss point j for each element. We write the gradient of the free volume at Gauss point j of element m, $\{(\nabla\xi)_j\}_m$ as

$$\{(\nabla\xi)_j\}_m \equiv \left[\left\{\left(\frac{\partial \xi}{\partial x_1}\right)^g_j\right\}_m, \left\{\left(\frac{\partial \xi}{\partial x_2}\right)^g_j\right\}_m, \left\{\left(\frac{\partial \xi}{\partial x_3}\right)^g_j\right\}_m\right], \quad j=1,2,\ldots,n_g.$$

Step 2a. Determine the first-order derivative of the free volume with respect to material coordinate x_1 at each node i of element m, $\left\{\left(\frac{\partial \xi}{\partial x_1}\right)^n_i\right\}_m$ by solving the set of linear equations

$$\sum_{i=1}^{n_n}(N_i)_j\left\{\left(\frac{\partial \xi}{\partial x_1}\right)^n_i\right\}_m = \left\{\left(\frac{\partial \xi}{\partial x_1}\right)^g_j\right\}_m, \quad j=1,2,\ldots,n_g.$$

Step 2b. Determine the first-order derivative of the free volume with respect to material coordinate x_2 at each node i of element m, $\left\{\left(\frac{\partial \xi}{\partial x_2}\right)^n_i\right\}_m$ by solving the set of linear equations

$$\sum_{i=1}^{n_n}(N_i)_j\left\{\left(\frac{\partial \xi}{\partial x_2}\right)^n_i\right\}_m = \left\{\left(\frac{\partial \xi}{\partial x_2}\right)^g_j\right\}_m, \quad j=1,2,\ldots,n_g.$$

Step 2c. Determine the first-order derivative of the free volume with respect to material coordinate x_3 at each node i of element m, $\left\{\left(\frac{\partial \xi}{\partial x_3}\right)^n_i\right\}_m$

by solving the set of linear equations

$$\sum_{i=1}^{n_n} (N_i)_j \left\{ \left(\frac{\partial \xi}{\partial x_3} \right)_i^n \right\}_m = \left\{ \left(\frac{\partial \xi}{\partial x_3} \right)_j^g \right\}_m , \quad j = 1, 2, \ldots, n_g.$$

The quantity $(N_i)_j$ denotes the value of the element level shape function associated with node i at Gauss point j for each element.

END DO (**End loop over the elements**)

By using the nodal averaging technique analogous to the method proposed by Zienkiewicz and Taylor (2000) and more recently Park et al. (2012), we can then calculate the refined value for the free volume gradient vector at each node of the body. Once this is done, we perform the following final step:

DO $m = 1, n_{el}$ (**Begin loop over the elements**)

Calculate the Laplacian of the free volume at Gauss point j of element m, $\left\{ (\nabla^2 \xi)_j \right\}_m$:

$$\left\{ (\nabla^2 \xi)_j \right\}_m = \sum_{i=1}^{n_n} \sum_{k=1}^{3} \left(\frac{\partial N_i}{\partial x_k} \right)_j \left\{ \left(\frac{\partial \xi}{\partial x_k} \right)_i^{n*} \right\}_m , \quad j = 1, 2, \ldots, n_g \qquad (14)$$

where $\left\{ \left(\frac{\partial \xi}{\partial x_k} \right)_i^{n*} \right\}_m$ represents the refined value of $\left\{ \left(\frac{\partial \xi}{\partial x_k} \right)_i^{n} \right\}_m$ with integers $i = 1, 2, \ldots, n_n$ and $k = 1, 2, 3$.

END DO (**End loop over the elements**)

Note: The nodal averaging technique is a standard method used in finite-element analysis, and it can be explained as follows: let node O denote a common node between four elements cf. Figure 2a. We are interested in finding the refined value of a variable λ at node O i.e. λ_O^*. Let λ_O^α represent the calculated value of λ at node O of element α where integers $\alpha = 1, 2, 3, 4$. With ω_α representing a geometric quantity associated with element α, the refined value of variable λ at node O, λ_O^* is defined to be

$$\lambda_O^* = \frac{\sum_{\alpha=1}^{4} \omega_\alpha \lambda_O^\alpha}{\sum_{\alpha=1}^{4} \omega_\alpha} .$$

3.3. Time-integration procedure

A central part of our finite-element program is the time-integration procedure for the constitutive model. With t denoting the current time, Δt is an infinitesimal time increment, and $\tau = t + \Delta t$. Recall that integers m represent the element index where $m = 1, 2, \ldots, n_{el}$, and integers j represent the Gauss point index where $j = 1, 2, \ldots, n_g$. The nodes of each element are labeled by integers $i = 1, 2, \ldots, n_n$.

In addition to the previous notations, we also use the following notations: Let s denote an arbitrary time. A quantity # at time s is denoted by $\#(s)$. A quantity # at Gauss point j of element m at time s is denoted by $\#(m, j, s)$. A quantity # at node i of element m at time s is denoted by $\#_i(m, s)$. A quantity # at Gauss point j of element m is denoted by $\#(m, j)$.

The main details of the time-integration procedure for the constitutive model are given as follows:

Given: (1) $\left\{ \mathbf{M}^\xi, \mathbf{K}^\xi(t), \mathbf{v}^\xi(t), \mathbf{f}^\xi(t) \right\}$.

Calculate: (a) $\left\{ \mathbf{K}^\xi(\tau), \mathbf{v}^\xi(\tau), \mathbf{f}^\xi(\tau) \right\}$.

Step A. Construct the global finite-element relation given by equation (11):

$$\mathbf{M}^\xi \dot{\mathbf{v}}^\xi(t) = -\mathbf{K}^\xi(t)\mathbf{v}^\xi(t) + \mathbf{f}^\xi(t). \tag{15}$$

Step B. Solve equation (15) to determine vector $\dot{\mathbf{v}}^\xi(t)$.

Step C. Assign the value of zero to the components of vector $\dot{\mathbf{v}}^\xi(t)$ which represent the free volume generation rate at time t at nodes located on $\mathcal{S}^d$.

Step D. Update the vector $\mathbf{v}^\xi(\tau)$:

$$\mathbf{v}^\xi(\tau) = \mathbf{v}^\xi(t) + \dot{\mathbf{v}}^\xi(t)\Delta t.$$

Step E. Using the steps listed in Section 3.2, calculate the free volume gradient $\nabla\xi(m, j, \tau)$ and the Laplacian of the free volume $\nabla^2\xi(m, j, \tau)$ for integers $m = 1, 2, \ldots, n_{el}$ and $j = 1, 2, \ldots, n_g$.

DO $m = 1, n_{el}$ (**Begin loop over the elements**)

DO $j = 1, n_g$ (**Begin loop over the Gauss points**)

Given: (1) $\{\,\mathbf{F}(m,j,t), \mathbf{F}(m,j,\tau)\,\}$; (2) $\{\,\mathbf{T}(m,j,t), \mathbf{F}^p(m,j,t)\,\}$; (3) $\{\,\dot\gamma(m,j,t), \gamma(m,j,t)\,\}$.

Calculate: (a) $\{\,\mathbf{T}(m,j,\tau), \mathbf{F}^p(m,j,\tau)\,\}$; (b) $\{\,\dot\gamma(m,j,\tau), \gamma(m,j,\tau)\,\}$.

Step 1. Calculate the elastic distortion $\mathbf{F}^e(t)$ and compute the polar decomposition of $\mathbf{F}^e(t)$:

$$\mathbf{F}^e(t) = \mathbf{F}(m,j,t)\,(\mathbf{F}^p(m,j,t))^{-1},$$

$$\mathbf{U}^e(t) = \sqrt{\mathbf{C}^e(t)} \quad \text{with} \quad \mathbf{C}^e(t) = (\mathbf{F}^e(t))^\top \mathbf{F}^e(t),$$

$$\mathbf{R}^e(t) = \mathbf{F}^e(t)\,(\mathbf{U}^e(t))^{-1}.$$

Step 2. Calculate the elastic stress $\mathbf{T}^e(t)$:

$$\mathrm{J}(t) = \det \mathbf{F}(m,j,t),$$

$$\mathbf{T}^e(t) = \mathrm{J}(t)\,(\mathbf{R}^e(t))^\top \mathbf{T}(m,j,t)\mathbf{R}^e(t).$$

Step 3. Update the plastic distortion $\mathbf{F}^p(m,j,\tau)$:

$$\mathbf{N}^p(t) = \frac{\operatorname{dev}\mathbf{T}^e(t)}{\|\operatorname{dev}\mathbf{T}^e(t)\|}, \quad \dot\xi(t) = \sum_{i=1}^{n_n} (N_i)_j\ \dot\xi_i(m,t),$$

$$\mathbf{D}^p(m,j,\tau) = \dot\gamma(m,j,t)\sqrt{\frac{1}{2}}\,\mathbf{N}^p(t) + \dot\xi(t)\left(\frac{1}{3}\right)\mathbf{I},$$

$$\mathbf{F}^p(m,j,\tau) = \{\,\mathbf{I} + \mathbf{D}^p(m,j,\tau)\Delta t\,\}\,\mathbf{F}^p(m,j,t).$$

Step 4. Calculate the elastic distortion $\mathbf{F}^e(\tau)$ and elastic Hencky strain $\mathbf{E}^e(\tau)$:

$$\mathbf{F}^e(\tau) = \mathbf{F}(m,j,\tau)\,(\mathbf{F}^p(m,j,\tau))^{-1},$$

$$\mathbf{U}^e(\tau) = \sqrt{\mathbf{C}^e(\tau)} \quad \text{with} \quad \mathbf{C}^e(\tau) = (\mathbf{F}^e(\tau))^\top \mathbf{F}^e(\tau),$$

$$\mathbf{E}^e(\tau) = (1/2)\ln \mathbf{C}^e(\tau) = \ln \mathbf{U}^e(\tau).$$

Step 5. Calculate the elastic stress $\mathbf{T}^e(\tau)$:

$$\mathbf{T}^e(\tau) = 2\mu\,(\operatorname{dev}\mathbf{E}^e(\tau)) + \kappa\,(\operatorname{trace}\mathbf{E}^e(\tau))\,\mathbf{I}.$$

Step 6. Update the Cauchy stress $\mathbf{T}(m,j,\tau)$:

$$\mathbf{R}^e(\tau) = \mathbf{F}^e(\tau)\,(\mathbf{U}^e(\tau))^{-1}, \quad \mathrm{J}(\tau) = \det \mathbf{F}(m,j,\tau),$$

$$\mathbf{T}(m,j,\tau) = (\mathrm{J}(\tau))^{-1}\,\mathbf{R}^e(\tau)\mathbf{T}^e(\tau)\,(\mathbf{R}^e(\tau))^{\top}.$$

Step 7. Calculate the free volume $\xi(m,j,\tau)$ and cohesion $c(\tau)$:

$$\xi(m,j,\tau) = \sum_{i=1}^{n_n} (N_i)_j\ \xi_i(m,\tau),$$

$$c(\tau) = c_o(m,j)\exp\left\{q\left(\xi(m,j,\tau) - \xi_o(m,j)\right)\right\}.$$

Step 8. Calculate the equivalent shear stress $\bar{\sigma}(\tau)$, hydrostatic pressure $\bar{p}(m,j,\tau)$, and the long-range interaction stress between defects $\bar{\sigma}_{int}(m,j,\tau)$:

$$\bar{\sigma}(\tau) = \sqrt{1/2}\ \|\mathrm{dev}\,\mathbf{T}^e(\tau)\|,$$

$$\bar{p}(m,j,\tau) = -(1/3)\,\mathrm{trace}\,\mathbf{T}^e(\tau),$$

$$\bar{\sigma}_{int}(m,j,\tau) = -\zeta s_{\xi 1}(\nabla^2\xi(m,j,\tau)).$$

Step 9. Calculate the driving force for plastic shearing $f^p(\tau)$:

$$f^p(\tau) = \bar{\sigma}(\tau)\ -\ \bar{\sigma}_{int}(m,j,\tau)\ -\zeta[\,s_{\xi 2}(\xi(m,j,\tau) - \xi_T)\ +\ \bar{p}(m,j,\tau)\,].$$

Step 10. Update the plastic shearing rate $\dot{\gamma}(m,j,\tau)$ and the plastic shear strain $\gamma(m,j,\tau)$:

$$\dot{\gamma}(m,j,\tau) = \dot{\gamma}_o\left(\frac{< f^p(\tau) >}{c(\tau)}\right)^{1/a},$$

$$\gamma(m,j,\tau) = \gamma(m,j,t)\ +\ \dot{\gamma}(m,j,\tau)\Delta t.$$

END DO (**End loop over the Gauss points**)

END DO (**End loop over the elements**)

Step F. Update the quantities $\mathbf{K}^{\xi}(\tau)$ and $\mathbf{f}^{\xi}(\tau)$:

$$\mathbf{K}^{\xi}(\tau) = \mathop{\mathbb{A}}_{m=1}^{n_{el}} \mathbf{K}^{\xi}_m(\tau), \quad \mathbf{f}^{\xi}(\tau) = \mathop{\mathbb{A}}_{m=1}^{n_{el}} \mathbf{f}^{\xi}_m(\tau).$$

The quantities $\mathbf{K}^{\xi}_{m}(\tau)$ and $\mathbf{f}^{\xi}_{m}(\tau)$ for the integers $m = 1, 2, \ldots, n_{el}$ are evaluated using equations (12) and (13), respectively, at time τ. The right-hand side of equations (12) and (13) are calculated using the Gaussian quadrature integration procedure.

Remark 1: For the present work, we have developed full-integration elements and used the B-bar method proposed by Simo et al. (1985) and Moran et al. (1990) to address the volumetric locking issue caused by the *nearly* incompressible response during plastic deformation. For stable time-integration, we ensure that the time increment Δt obeys the restriction $\Delta t \leq \min\left(L_e/C_d,\, (1/2)L_e^2/K\right)$ where L_e is the smallest characteristic length of an element in the mesh, and C_d is the dilatational wave speed of the material. To speed up the computations, we use mass scaling. Furthermore, all of our numerical simulations were conducted under *quasi-static* conditions by ensuring that $KE \lll IE$ where KE and IE represents the total kinetic energy and the total internal energy, respectively, of the sample during deformation.

4. Numerical simulations

4.1. Material parameters and verification of the presently developed finite-element code

Before verifying our presently developed finite-element code, it is important to briefly depict a method for determining the value for the gradient energy coefficient, $s_{\xi 1}$ which is responsible for introducing the material length scale in our constitutive model. Note that the material parameters used in our simulations are generally for Zr-based metallic glasses.

Following Zheng and Li (2009) and Zheng and Shen (2009), we take the gradient energy coefficient, $s_{\xi 1} = \Gamma l_c$ where Γ is the fracture surface energy (units of energy per unit area), and l_c the fracture process zone size (units of length). From Kumar et al. (2011), we take $l_c \approx 100\mu m$. By choosing $\Gamma = 9\,\mathrm{Jm}^{-2}$ (Dubach et al., 2009), we obtain $s_{\xi 1} = 900\,\mu\mathrm{J/m}$. For values of the other material parameters in the constitutive model, we use the list of material parameters employed by Thamburaja (2011) given in Table 1[7].

[7]In our continuum-based numerical simulations, we have imposed strain-rates which are typically encountered in physical experiments. Since the stress-strain responses at

Table 1: List of material parameters at room temperature.

$\mu = 35.7$ GPa	$\kappa = 166.7$ GPa	$\xi_T = 0.06\%$
$\zeta = 0.02$	$\nu_o = 323$ s^{-1}	q = -250
$s_{\xi 2} = 2800$ GJ/m^3	$s_{\xi 3} = 240$ GJ/m^3	$\varphi = 0.15$
$\dot{\gamma}_o = 0.00173$ s^{-1}	$a = 0.02$	$c_o = 1.0$ GPa

For convenience, we shall recap the physical meaning of the other material parameters listed in Table 1: (a) μ and κ are the shear and bulk moduli, respectively; (b) ξ_T is the fully-annealed (thermal equilibrium) free volume; (c) ζ is the free volume creation coefficient; (d) ν_o is a constant reference frequency for free volume relaxation and diffusion; (e) q is the cohesion softening coefficient; (d) $s_{\xi 2}$ is the defect energy coefficient; (e) $s_{\xi 3}$ is the resistance to free volume generation due to mechanisms other than plastic shearing; (f) φ is a geometric factor (Spaepen, 1977); (g) $\dot{\gamma}_o$ is the reference plastic shearing rate; (h) a is the plastic strain-rate sensitivity parameter; and (i) c_o is the initial cohesion.

Remark 2: Using the values for the material parameters listed in Table 1, we perform a simple compression finite-element simulation of a large-volume sample[8] using a single three-dimensional brick element under *homogeneous* deformation conditions. The stress-strain response and the variation of free volume with respect to applied strain obtained from this simulation is plotted in Figures 2b and 2c, respectively. From the results shown in Figures 2b and 2c, it can be seen that the post-yield plastic deformation consist of a strain-softening response followed by a saturation of the stress with continued deformation. The strain-softening response is due to the creation of free volume, and once the creation of free volume is offset by free volume structural relaxation, a steady-state free volume is attained in the sample and the stress saturates with applied deformation.

Consider the initially undeformed sample shown in Figure 3a which has

low-homologous temperatures are (nearly) rate-independent cf. Lu (2002), we have used a relatively low strain-rate sensitivity of $a = 0.02$ to model the nearly rate-insensitive behavior of metallic glasses.

[8]In large-volumed (bulk) samples, we can neglect the effect of the non-local term $\nabla^2\xi$ in our calculations.

dimensions of 408nm by 816nm by 17nm when measured along axes-1, 2 and 3, respectively. The undeformed sample is assumed to be initially in the fully-annealed state i.e. $\xi_o = \xi_T$ throughout the undeformed sample, and initially stress-free. We mesh the sample shown in Figure 3a using 16000 continuum three-dimensional hexahedral elements, and Figures 3b and 3c represent the different views of the initially undeformed finite-element mesh of the sample shown in Figure 3a. Using the Abaqus (2012) and presently developed finite-element implementation of the constitutive model presented in Section 2, we perform a plane-strain compression simulation of the sample shown in Figure 3a[9]. The following loading conditions and macroscopic/microscopic boundary conditions are imposed on the sample shown in Figure 3a: (a) the nodes located on the top surface are given a displacement profile along axis-2 to match the desired testing rate, (b) the nodes located on the bottom surface are prevented from motion along axis-2, (c) the nodes located on the external surfaces of the sample which have an outward unit normal vector parallel to axis-3 are prevented from motion along axis-3, and (d) $\nabla\xi \cdot \mathbf{n} = 0$ at the external surfaces of the sample. Additional nodal displacement boundary conditions are also imposed on the sample to suppress rigid body motions.

Both the plane-strain compression simulations were conducted at a constant (absolute) true strain rate of $1 \times 10^{-3}\ s^{-1}$ using the material parameters listed in Table 1. An imperfection is introduced in the sample shown in Figure 3a by giving a few elements a lower value of initial cohesion (0.98 GPa) cf. Figures 3b and 3c. This imperfection will serve as nucleation sites for shear localization (Anand and Su, 2005). For convenience, we shall label the numerical simulation using the Abaqus (2012) finite-element implementation as Simulation A, and label the numerical simulation using the presently developed finite-element implementation as Simulation B.

Figure 4 shows the absolute-valued nominal stress vs. nominal strain response obtained from Simulations A and B. Note that the stress-strain curves determined from Simulations A and B qualitatively match the major features of the compression stress-strain curves determined from the molecular dynamics simulations of small-volume metallic glass samples cf. Shi and Falk (2006). From Figure 4, we can also see that the stress-strain re-

[9]In the Abaqus (2012) finite-element simulations, we have used reduced integration elements and calculated $\nabla^2\xi$ using a finite-difference scheme. For more details regarding the Abaqus (2012) implementation of the constitutive model, refer to Thamburaja (2011).

sponse obtained from Simulation B accurately reproduces the stress-strain response obtained from Simulation A. Furthermore, the contours of the plastic shear strain in the sample determined from Simulations A and B at an applied nominal strain of 4.2% match each other accurately, and the predicted fully-developed shear band width from both numerical implementations are identical as well cf. the contour plots shown in Figure 4. It is also worth noting from the contour plots drawn in Figure 4 that the predicted fully-developed shear band width of approximately 84nm agrees well with the experimentally-observed shear band widths of $10 \sim 100$nm (Li et al., 2002; Yang et al., 2005).

Therefore, we have verified the presently-developed finite-element implementation of the constitutive model presented in Section 2, and we shall perform all ensuing numerical simulations using the presently-developed finite-element algorithm.

4.2. Mechanical response of small-volume amorphous metal samples in tension

Consider an undeformed nanotensile test sample with the geometry shown in Figure 5a. The undeformed nanotensile test sample is assumed to be initially in the fully-annealed state i.e. $\xi_o = \xi_T$ throughout the undeformed sample, and initially stress-free. With regards to test sample shown in Figure 5a, we also make the following modeling assumptions: (a) the free volume in the grip sections is always fixed at ξ_T; and (b) the grip sections only deform *elastically* whereas the gage section is able to undergo *elastic-plastic* deformations.

For simplicity, we only model the gage section of the test sample. Figure 5b shows the initially undeformed geometry of the test sample's gage section. The cuboid-shaped gage section shown in Figure 5b has a length l (measured along axis-3), width w (measured along axis-1) and breadth w (measured along axis-2) i.e. the gage section of the test sample shown in Figure 5b has a square cross section. For our numerical simulations, we have taken $l/w = 8$ following the experiments of Jang and Greer (2010). The top (bottom) surface of the test sample's gage section cf. Figure 5b coincides with the interface between the top (bottom) grip section and the gage section of the test sample shown in Figure 5a.

The nanotensile sample's gage section shown in Figure 5b is then meshed using 1728 continuum three-dimensional hexahedral elements cf. Figure 5c,

and each element has eight nodes and eight Gauss points. All of our numerical simulations were conducted using the initially undeformed finite-element mesh shown in Figure 5c.

The following displacement/macroscopic boundary conditions are then imposed on the finite-element mesh shown in Figure 5c to simulate a simple tension loading condition: (a) the nodes located on the bottom surface are prevented from motion along axis-3; and (b) the nodes located on the top surface are given a displacement profile along axis-3 to match the desired testing rate. Additional nodal displacement boundary conditions are also imposed on the sample to suppress rigid body motions.

We also impose the following *microscopic* boundary conditions on the finite-element mesh shown in Figure 5c :

• MBC1: The free volume at the top (bottom) surface is always fixed at ξ_T since the top (bottom) surface is constantly in contact with the top (bottom) grip section i.e. $\xi = \xi_T \implies \dot{\xi} = 0$ at the nodes located on the top and bottom surfaces.

• MBC2: No free volume is allowed to enter or leave through the lateral/free surfaces i.e. $\nabla\xi \cdot \mathbf{n} = 0$ at the nodes located on the lateral/free surfaces.

Hence, the MBC1 and MBC2 microscopic boundary conditions represent a Dirichlet-type and Neumann-type boundary condition for the free volume, respectively cf. Section 3.1.

All of our simple tension simulations were conducted at a constant (absolute) true strain rate of $1 \times 10^{-4}\ s^{-1}$ using the material parameters listed in Table 1. Furthermore, the Gauss points of an element at the center of the finite-element mesh shown in Figure 5c were given a lower value of initial cohesion (0.94 GPa) to serve as nucleation sites for shear localization.

In this work, we have simulated the mechanical response of three different gage section (sample) sizes: $l = 120$nm and $w = 15$nm (Simulation A1), $l = 96$nm and $w = 12$nm (Simulation B1), and $l = 72$nm and $w = 9$nm (Simulation C1) cf. Table 2 for a summary of the sample sizes modeled in our simulations. With $\bar{l}_{md}$ denoting the characteristic sample length used in the molecular dynamics simulations of Li and Li (2006) and Pang et al. (2010) and $\bar{l}_{exp}$ denoting the characteristic sample length used in the experiments of Jang and Greer (2010) and Tian et al. (2012), note that $\bar{l}_{md} < \bar{l}_{sim} < \bar{l}_{exp}$ where $\bar{l}_{sim}$ represents the characteristic length of the nanotensile specimens

simulated in the present work[10]. Furthermore, since the sample sizes modeled in this work are also similar to sample sizes modeled in the simulations of Homer and Schuh (2010), we neglect the effect of surface tension in our simulations.

Table 2: Sample sizes modeled in the finite-element simulations.

Simulation	initial length (nm)	initial width (nm)	initial breadth (nm)
A1, A2, D	120	15	15
B1, B2, E	96	12	12
C1, C2, F	72	9	9

From the deformed finite-element mesh of the sample modeled in Simulations A1, B1 and C1 cf. Figure 6, we can conclude that each sample has undergone *homogeneous* deformation in a *macroscopic* sense i.e. at an applied true strain of 8.3%, the cross sectional area of each sample along the loading axis (axis-3) can still be treated as being uniform. Furthermore, there is no evidence of shear banding in each deformed sample.

Remark 3: Since the nanotensile sample sizes modeled in this work have a characteristic length of $10 \sim 100$nm, it is unsurprising that sample size-scale shear localization does not occur since the calculated incubation length scale necessary for shear band maturation is about 100nm for Zr-based metallic glasses (Shimizu et al., 2006).

The stress-strain response obtained from Simulations A1, B1 and C1 are shown in Figure 6. We can see that the post-yield stress-strain response determined from Simulations A1 B1 or C1 cf. Figure 6 clearly demonstrates conventional metal-like *work hardening* characteristics although dislocation-based activities do not occur in amorphous metals. Furthermore, the rate of strain-hardening is also predicted to *increase* with *decreasing* sample size. This trend is very similar to crystalline metals experiencing dislocation-based energetic gradient hardening effects (Gurtin et al., 2007; Niordson and Legarth, 2010) although geometrically necessary dislocations are also not present in amorphous metals. Hence, the stress-strain curves shown in

[10]The dimension of the sample which is important in determining the transition between shear localization and homogeneous behavior in metallic glass samples is the length cf. the analytical calculations in Volkert et al. (2008) and Jang and Greer (2010).

Figure 6 are markedly different to the strain-softening-type stress-strain response typically exhibited by bulk amorphous metals.

Let $\mathrm{V} = \int_{\mathcal{R}} \mathrm{dV}$ represent the volume of a sample in the *reference* configuration. From the contours of the plastic shear strain and free volume in the deformed finite-element mesh of each sample cf. Figure 7, we can deduce that the *average* plastic shear strain and free volume in the sample, respectively defined as

$$\bar{\gamma} = \frac{1}{\mathrm{V}} \int_{\mathcal{R}} \gamma \ \mathrm{dV} \quad \text{and} \quad \bar{\xi} = \frac{1}{\mathrm{V}} \int_{\mathcal{R}} \xi \ \mathrm{dV},$$

reduces with *decreasing* sample size. Hence, we can also conclude from Simulations A1, B1 and C1 that nanotensile amorphous metal specimens become more *resistant* to plastic deformation and free volume creation with *reducing* sample size. It is also important to note that although the *initial* free volume distribution within each undeformed sample was assumed to be homogeneous, plastic deformation causes the development of a markedly *heterogeneous* free volume distribution within each deformed sample cf. Figure 7.

To *qualitatively* compare the results from our theoretical and numerical approach to physical experimental data cf. the experimental results shown in Figure 1, we perform a cyclic tension finite-element simulation using the amorphous metal sample modeled in Simulation A1/B1/C1, and label this new finite-element simulation as Simulation D1/E1/F1. Starting from an initially undeformed state, we impose the following deformation history for the cyclic tension simulations: *Loading step 1.* Each sample is deformed to a true strain of 2.96%; *Unloading step 1.* At a true strain of 2.96%, reverse loading is imposed until zero applied stress is attained in each sample; *Loading step 2.* Once zero applied stress is attained, each sample is then deformed to a true strain of 5.83%; *Unloading step 2.* At a true strain of 5.83%, reverse loading is imposed until zero applied stress is attained in each sample; *Loading step 3.* Once zero applied stress is attained, each sample is then continuously deformed in tension until elastic-plastic deformation is observed again.

The initially undeformed finite-element mesh shown in Figure 5c was used to conduct Simulations D1, E1 and F1. The cyclic tension stress-strain curves determined from Simulations D1, E1 and F1 are shown in Figure 8. From Figure 8, we can see that the simulated cyclic tension stress-strain curves are qualitatively similar to the experimental results of Jang and Greer (2010) shown in Figure 1 i.e. for each stress-strain curve shown in Figure 8a, we can determine that: (a) the residual plastic strain (the distance from the

origin to the intersection of the stress-strain curve and the true strain axis) *increases* with increasing loading-unloading steps, and (b) the yield stress in each subsequent loading step increases to the plastic flow stress of the previous loading step. Thus, our finite-element simulations clearly show that the amorphous metal samples modeled in Simulations D1, E1 and F1 have been work-hardened.

In conclusion, our constitutive model and numerical simulations are able to *qualitatively* reproduce the work hardening stress-strain response observed in physical experiments (Jang and Greer, 2010; Tian et al., 2012) and molecular dynamics simulations (Li and Li, 2006; Pang et al., 2010) cf. Figure 1.

4.3. Effect of microscopic boundary conditions on the deformation behavior of amorphous metals

As the sample volume becomes smaller, the effect of boundary conditions become more important. To study the effect of microscopic boundary conditions on the deformation behavior of small-volume amorphous metals, we perform the following calculations: instead of applying the MBC1 microscopic boundary condition in our new numerical simulations, we impose the Neumann-type boundary condition $\nabla\xi \cdot \mathbf{n} = 0$ at the nodes located on the top and bottom surfaces of the amorphous metal sample modeled in Simulation A1/B1/C1, and label this new finite-element simulation as Simulation A2/B2/C2.

Simulations A2, B2 and C2 were conducted using the initially undeformed finite-element mesh shown in Figure 5c and also the material parameters listed in Table 1. As done previously, the Gauss points of an element at the center of the finite-element mesh shown in Figure 5c were given a lower value of initial cohesion (0.94 GPa) to serve as nucleation sites for shear localization.

The monotonic tensile stress-strain curves obtained from Simulations A2, B2 and C2 are plotted in Figure 8b along with the previously-determined stress-strain curves obtained from Simulations A1, B1 and C1. From Figure 8b, we can see that the stress-strain response obtained from Simulations A2, B2 and C2 are identical. The uniform contours of the plastic shear strain and free volume throughout each deformed sample cf. Figure 9 show that the samples modeled in Simulations A2, B2 and C2 have undergone homogeneous deformations. Furthermore, as shown by the contour plots drawn in Figure 9, no evidence of shear banding was observed in each deformed sample cf. the explanation given in Remark 3.

By redirecting our attention back to the stress-strain curves shown in Figure 8b, we can see that the stress-strain curve determined from Simulations A2, B2 or C2 show the classical post-yield strain-softening response typically exhibited by amorphous metals (Anand and Su, 2005; Thamburaja, 2011). From the comparison between the stress-strain curve obtained from Simulation A1/B1/C1 to the stress-strain curve obtained from Simulation A2/B2/C2 cf. Figure 8b, we can conclude that the characteristics of the post-yield i.e. strain-softening vs. strain-hardening stress-strain response is determined by the types of microscopic boundary conditions imposed on the small-volume amorphous metal sample (more on this later). Furthermore, the post-yield stress-strain response of a small-volume amorphous metal sample is also significantly influenced by the types of microscopic boundary conditions imposed on the sample cf. Figure 8b.

Recall that the undeformed amorphous metal samples modeled in our finite-element simulations contain an initially uniform free volume distribution. By comparing the contour plots shown in Figure 7 to the contour plots shown in Figure 9, we can also conclude that the free volume distribution within the plastically deformed samples modeled in Simulations A1, B1 and C1 cf. Figure 7 become heterogeneous due to the application of the MBC1 microscopic boundary condition.

To study the effect of free volume heterogeneity within a sample, we analyze the evolution equation for the plastic shear strain in the *rate-independent* limit i.e. as $a \to 0$, and obtain the *yield function*

$$\bar{\sigma} - \zeta \bar{p} = \bar{\sigma}_{int} + \zeta s_{\xi 2}(\xi - \xi_T) + c. \tag{16}$$

The collective term on the right-hand side of equation (16) represents the *total resistance* to plastic deformation. Note that the total resistance to plastic deformation contains local terms and also the non-local quantity $\bar{\sigma}_{int} = -\zeta s_{\xi 1}(\nabla^2 \xi)$ i.e. the interaction stress. Concentrating on the one-dimensional stress-strain response and using the value for the free volume creation parameter given in Table 1 allows us to reduce equation (16) to

$$\bar{\sigma} = \bar{\sigma}_{int} + \zeta s_{\xi 2}(\xi - \xi_T) + c. \tag{17}$$

Taking the time-derivative of equation (17) and using equation $\dot{c} = q\, c\, \dot{\xi}$ results in

$$\dot{\bar{\sigma}} = \dot{\bar{\sigma}}_{int} + (\zeta s_{\xi 2} + q\, c)\, \dot{\xi}. \tag{18}$$

With increasing sample volume i.e. as $l \to \infty$, the quantities $\bar{\sigma}_{int} \to 0$ and $\dot{\bar{\sigma}}_{int} \to 0$. If the free volume remains uniformly distributed within a sample during deformation e.g. see the contour plots obtained from Simulations A2, B2 and C2 shown in Figure 9, we have $\bar{\sigma}_{int} = 0$ and $\dot{\bar{\sigma}}_{int} = 0$ at all times.

For Simulations A1, B1 and C1, we can see that the created heterogeneity in the free volume field within each deformed sample cf. Figure 7 has resulted in the generation of significantly large interaction stresses cf. Figure 10a. As shown in Figure 10a, the long-range interaction stress between defects, $\bar{\sigma}_{int}$ throughout each plastically deformed sample is *positive-valued*. This implies that during plastic deformation, each point within the sample modeled in Simulations A1, B1 and C1 experiences a *positive* rate of change of interaction stress i.e. $\dot{\bar{\sigma}}_{int} > 0$. Thus, from equation (17), we can see that a *positive* rate of change of the interaction stress i.e. $\dot{\bar{\sigma}}_{int} > 0$ *increases* the total resistance to plastic deformation (with all other terms on the right-hand side of equation (17) being constant).

Note that for Simulations A2, B2 and C2, we have $\dot{\bar{\sigma}}_{int} = 0$ as mentioned previously. For these cases, equation (18) reduces to

$$\dot{\bar{\sigma}} = (\zeta s_{\xi 2} + q\, c)\, \dot{\xi}. \tag{19}$$

From Figure 9, we can also see that free volume is *created* during plastic deformation. Since $\dot{\bar{\sigma}} < 0$ during plastic deformation cf. Figure 8b, we can use equations $c = c_o \exp\{q\,(\xi - \xi_o)\}$, (19) and the material parameters listed in Table 1 to conclude that $\zeta s_{\xi 2} < -q\, c$ for the free volume values shown in Figure 9.

Hence, the work hardening stress-strain response observed in Simulations A1, B1 and C1 cf. Figure 6 can be explained as follows: the MBC1 microscopic boundary condition creates a heterogeneous free volume distribution within each deformed sample, and the creation of free volume ($\dot{\xi} > 0$) during plastic deformation ($\dot{\gamma} > 0$) is also accompanied with the fulfillment of the condition $\dot{\bar{\sigma}}_{int} > -(\zeta s_{\xi 2} + q\, c)\, \dot{\xi}$ for the free volume values shown in Figure 7. Consequently, this will result in the work hardening behavior ($\dot{\bar{\sigma}} > 0$) during plastic deformation cf. equation (18).

Remark 4: Our combined continuum-based theoretical and computational effort have shown that monolithic amorphous metals are capable of exhibiting a work hardening response during plastic deformation if the following conditions are satisfied: (1) the sample volume is small enough, and (2) the appropriate microscopic boundary conditions are imposed on the sample.

4.4. Cyclic deformation of small-volume metallic glass samples

Recall that the sample size modeled in Simulation A1, B1 and C1 is the same as the sample size modeled in Simulation D1, E1 and F1, respectively. The free volume distribution in the sample modeled in Simulation A1/B1/C1 cf. Figure 7 is also the same as the free volume distribution in the sample modeled in Simulation D1/E1/F1 at (a) *Instant A*: the end/beginning of *Loading/Unloading step 2*, and (b) *Instant B*: a true strain of 5.83% when plastic flow starts to occur during *Loading step 3*. Therefore, our numerical simulations show that the free volume distribution in each sample do not visibly change during elastic loading and unloading, and with regards to Simulations D1, E1 and F1, the yield stress in each subsequent loading step increases to the flow stress of the previous loading step[11].

The free volume generation during the elastic loading and unloading steps of Simulations D1, E1 and F1 can also be investigated by the following analysis: assuming that the free volume generation term due to the effect of hydrostatic pressure can be neglected (Yang et al., 2006), we can then write the free volume evolution equation during the elastic loading and unloading steps as

$$\dot{\xi} \approx K\left(\nabla^2 \xi\right) - \left(\frac{\nu_* s_{\xi 2}}{s_{\xi 3}}\right)(\xi - \xi_T). \tag{20}$$

Since ξ_T is a constant, equation (20) can be rewritten as

$$\dot{\overline{(\xi - \xi_T)}} \approx K\left(\nabla^2(\xi - \xi_T)\right) - \left(\frac{\nu_* s_{\xi 2}}{s_{\xi 3}}\right)(\xi - \xi_T) \tag{21}$$

where $K = \nu_*(s_{\xi 1}/s_{\xi 3})$ and $\nu_* = \nu_o\sqrt{\exp(-\varphi/\xi)}$ as mentioned previously.

In one dimensions, the characteristic time-scales for the free volume diffusion and relaxation, $\bar{\tau}_D$ and $\bar{\tau}_R$, respectively, can be obtained from equation (21):

$$\bar{\tau}_D = \sqrt{\exp(\varphi/\xi)}\left(\frac{l_h^2 s_{\xi 3}}{s_{\xi 1}\nu_o}\right), \quad \bar{\tau}_R = \sqrt{\exp(\varphi/\xi)}\left(\frac{s_{\xi 3}}{s_{\xi 2}\nu_o}\right) \tag{22}$$

where l_h is the half-length of the sample i.e. $l_h = l/2$. As a conservative approach, we choose the specimen size modeled in Simulations C1/F i.e.

[11] The contours of the long-range interaction stress within the sample modeled in Simulation A1/B1/C1 cf. Figure 10a is also the same as the contours of the long-range interaction stress within the sample modeled in Simulation D1/E1/F1 at *Instant A* and *Instant B*.

$l_h = 41.6$nm, and plot the variation of $\bar{\tau}_D$ and $\bar{\tau}_R$ with respect to free volume in Figure 10b. Next, we define the characteristic time-scale for the numerical simulations, $\bar{\tau}_S \equiv 1/\dot{\epsilon}_s$ where $\dot{\epsilon}_s = 1 \times 10^{-4}\ s^{-1}$ represents the applied deformation rate in the numerical simulations. We also plot the value of $\bar{\tau}_S$ in Figure 10b for comparison purposes. Considering that $\bar{\tau}_D \gg \bar{\tau}_S$ and $\bar{\tau}_R \gg \bar{\tau}_S$ for the values of free volume shown in Figure 7, the effect of free volume diffusion and relaxation can be disregarded for time-scales involving our numerical simulations, and equation (1) will be further reduced to $\dot{\xi} \approx \zeta\dot{\gamma}$ since the term describing the hydrostatic pressure-induced free volume generation can also be neglected (Yang et al., 2006) i.e. the free volume is set by *plastic* deformation[12]. Thus, with regards to Simulations D1, E1 and F1, we can ascertain that the distribution of the free volume and the total resistance to plastic deformation (the collective term on the right-hand side of equation (16)) within the samples do not change significantly during the elastic loading & unloading of the samples, and this in turn will cause the yield stress in each subsequent loading step to increase to the plastic flow stress of the previous loading step cf. the stress-strain curves shown in Figure 8a.

5. Conclusion

In the present work, we have implemented the finite-deformation, strain gradient plasticity-based constitutive model for amorphous metals derived by Thamburaja (2011) into a self-developed finite-element code. By imposing different types of microscopic boundary conditions i.e. boundary conditions involving the free volume/defect density on small-volume amorphous metal samples of various sizes, we have shown through our finite-element simulations that amorphous metals are *capable* of exhibiting a work hardening stress-strain response if (a) the sample volume is small enough, and (b) the appropriate microscopic boundary conditions are imposed on the sample.

To the best of our knowledge, the present combined continuum mechanics-based theoretical and numerical effort is the first of its kind to show that work hardening response can be exhibited by intrinsically strain-softening materials like monolithic amorphous metals.

[12]Since $\bar{\tau}_R < \bar{\tau}_D$ cf. Figure 10b, we can conclude that for the sample sizes modeled in this work, structural relaxation has a greater effect on free volume generation compared to free volume diffusion.

As part of our future work, we intend to use our newly-developed numerical tool to study how the deformation behavior of small-volume metallic glass specimens is affected by the interaction of different microscopic boundary conditions and the heterogeneous initial free volume distribution in metallic glass specimens caused by the quenching of annealed samples cf. the work of Li et al. (2013). As a preview to the effect of initial free volume distribution on the deformation behavior of small-volume metallic glass samples, please refer to the analytical calculations performed in Appendix A.

Acknowledgements

PT would like to acknowledge the funding received from the Arus Perdana program of UKM under Grant No. AP-2012-022. JL would like to acknowledge the financial support provided by the Graduate Student Fellowship of the National University of Singapore (NUS).

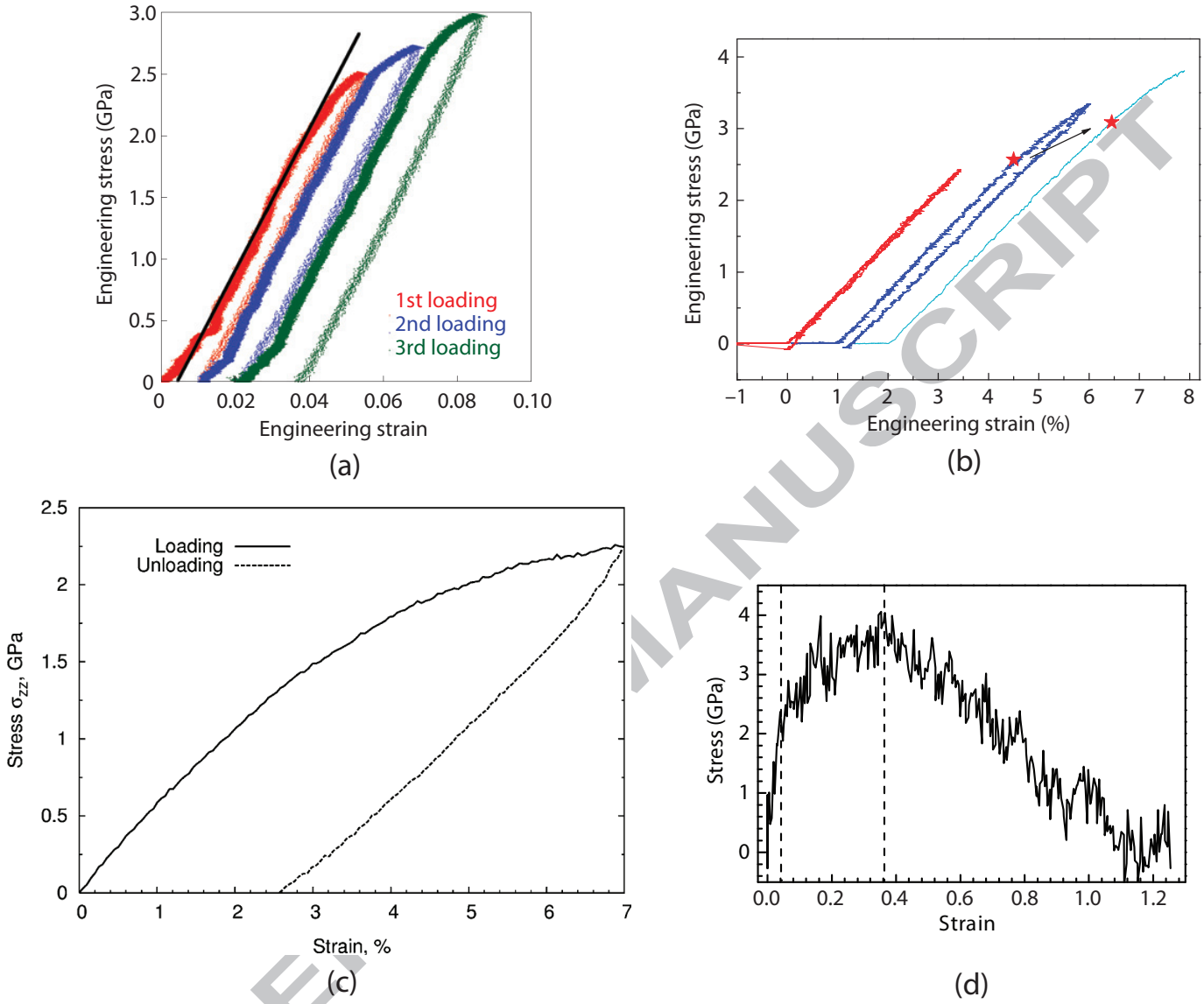

Figure 1: Cyclic tensile stress-strain curves obtained from the multiple loading and unloading of nanotensile metallic glass samples taken from the experiments of (a) Jang and Greer (2010), and (b) Tian et al. (2012). A molecular dynamics-determined tensile stress-strain response of a nano-sized metallic glass sample obtained from the simulations of (c) Li and Li (2006), and (d) Pang et al. (2010).

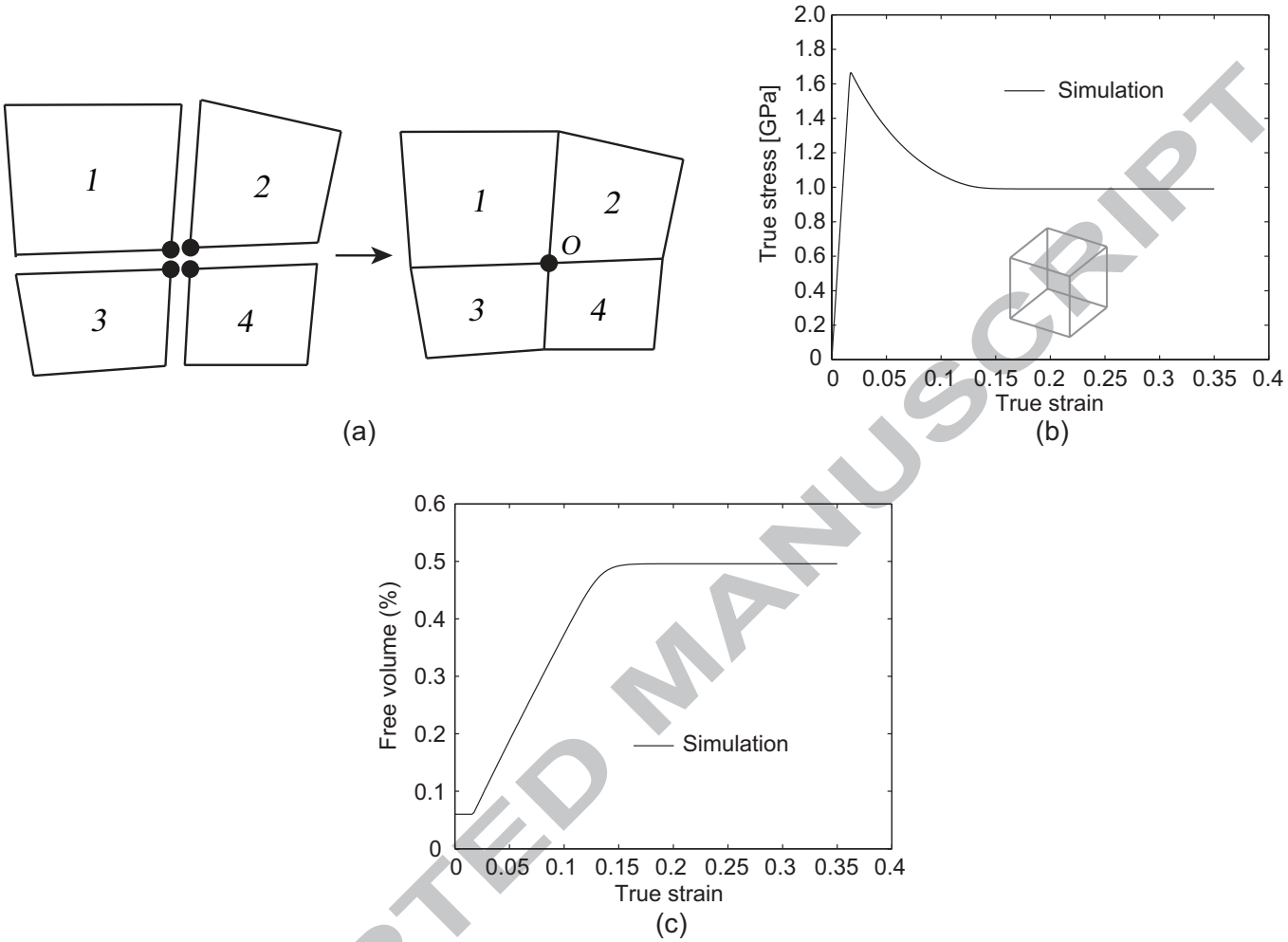

Figure 2: (a) The schematic diagram of four elements sharing a common node which we denote as node O. (b) Homogeneous stress-strain response obtained from a simple compression finite-element simulation conducted at an (absolute-valued) true strain rate of 1×10^{-4} s^{-1}, and (b) the corresponding variation of free volume with respect to applied strain. Absolute values of stress and strain are plotted. Shown inset of Figure 2b is the initially-undeformed single three-dimensional element used to perform the simple compression simulation.

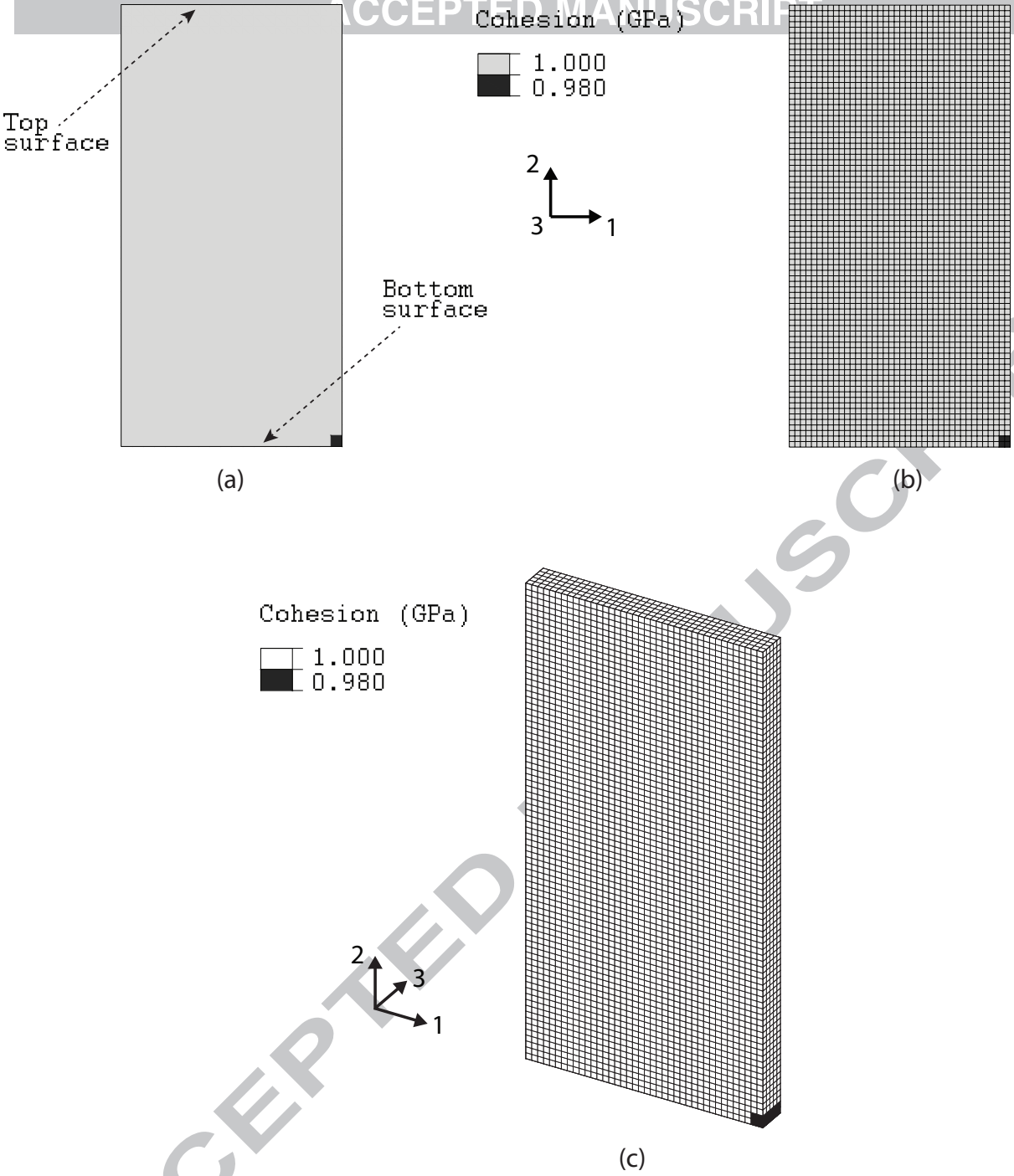

Figure 3: (a) The plane view of an initially undeformed sample with dimensions of 408nm by 816nm by 17nm when measured along axes-1, 2 and 3, respectively; (b) the plane view of the initially undeformed finite-element mesh of the sample shown in Figure 3a; and (c) the three-dimensional view of the initially undeformed finite-element mesh of the sample shown in Figure 3a. We have meshed the sample using 16000 continuum three-dimensional hexahedral elements. Also shown in Figures 3a, 3b and 3c are the contours of the initial cohesion in the sample.

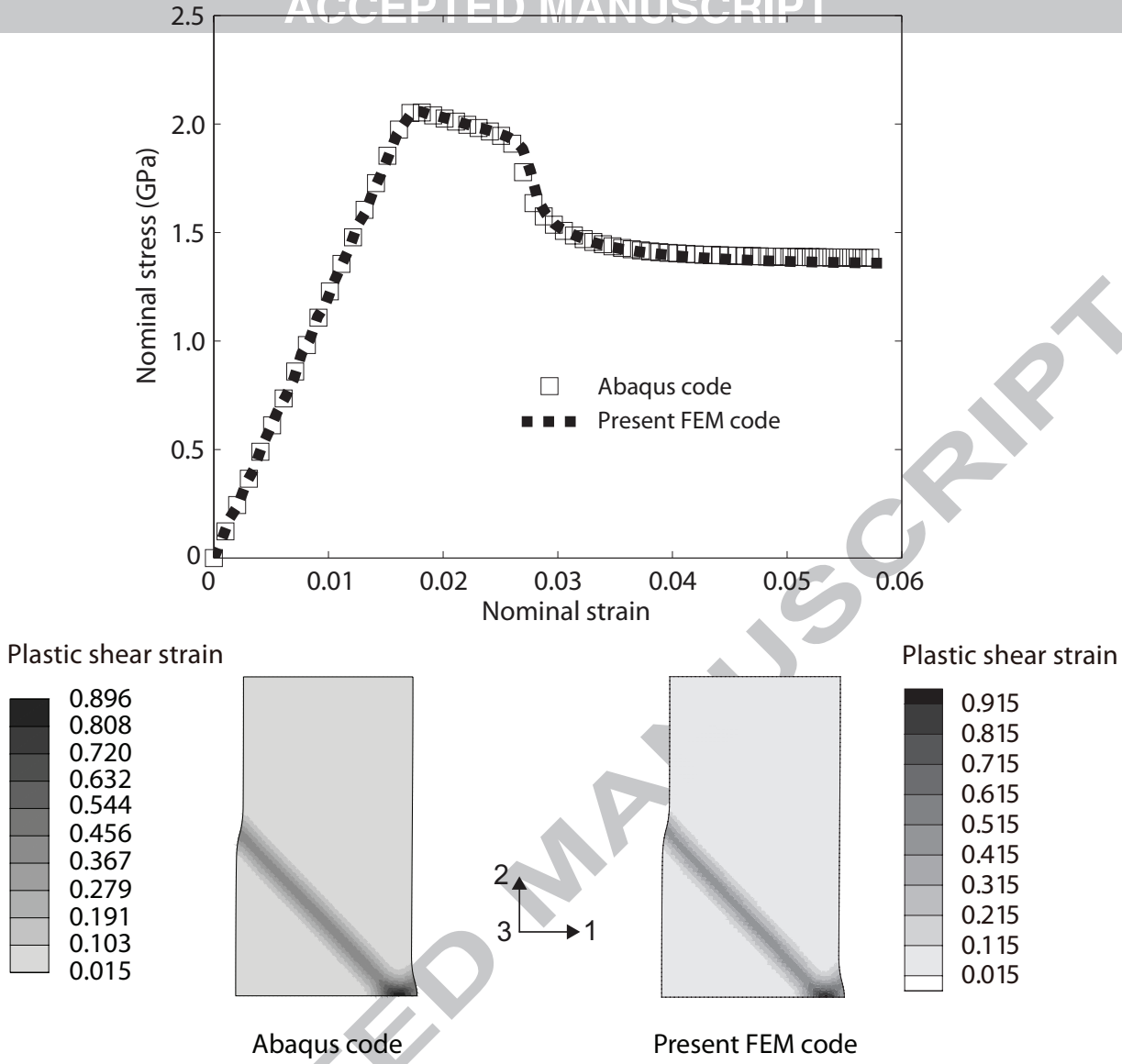

Figure 4: The absolute-valued nominal stress vs nominal strain response obtained from Simulations A and B, and the plastic shear strain contours in the sample shown in Figure 3a at an applied nominal strain of 4.2% obtained from Simulations A and B. Simulation A was conducted using the Abaqus (2012) finite-element implementation of the constitutive model whereas Simulation B was conducted with the constitutive model implemented into the presently-developed finite-element code. Note that the stress-strain responses shown in the present figure qualitatively match the major features of the compression stress-strain curves determined from molecular dynamics simulations of small-volume metallic glass samples cf. Shi and Falk (2006).

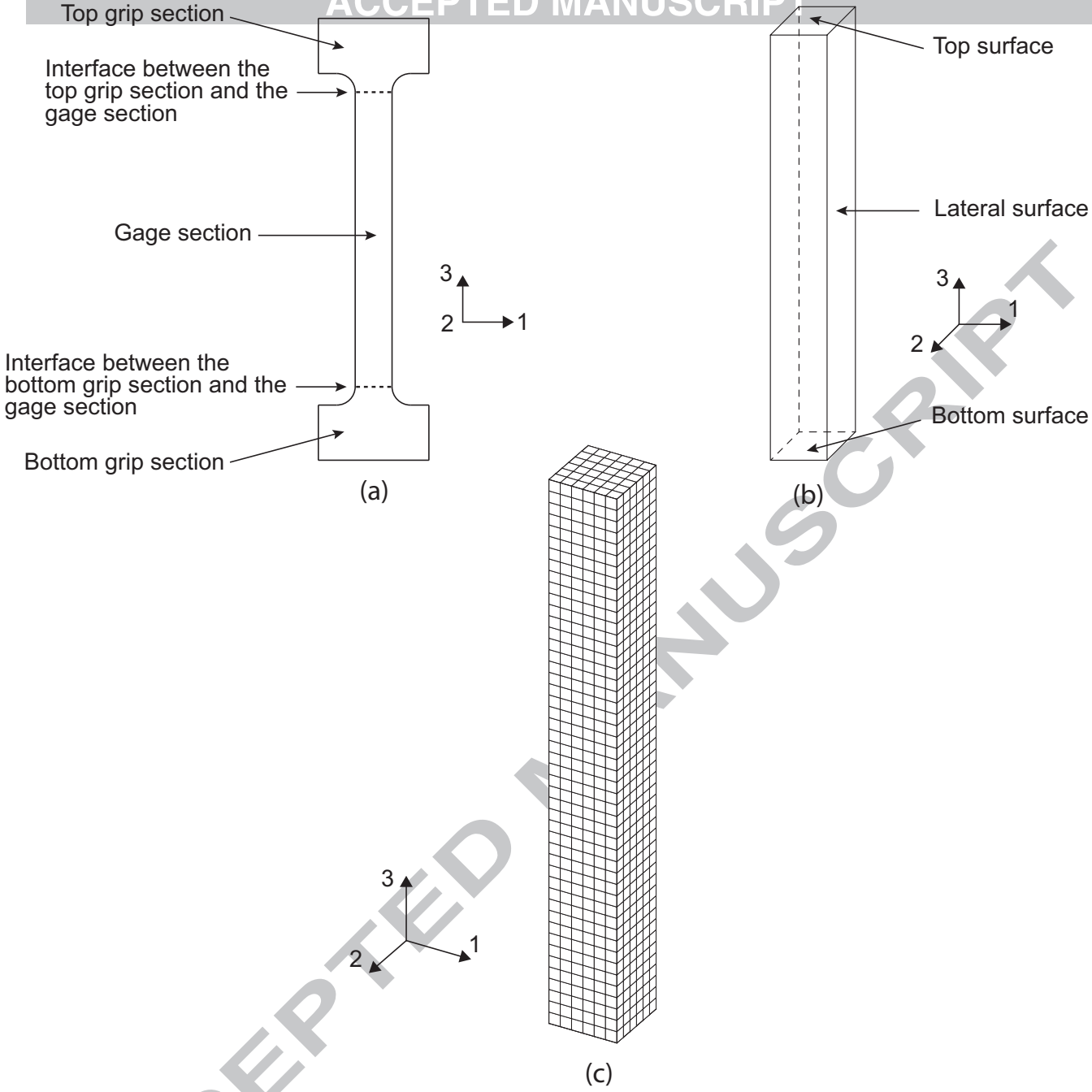

Figure 5: (a) Schematic diagram of an undeformed nanotensile specimen. (b) The initially undeformed gage section of the nanotensile specimen shown in Figure 5a, and (c) the initially undeformed finite-element mesh of the nanotensile specimen's gage section shown in Figure 5b, consisting of 1728 continuum three-dimensional hexahedral elements.

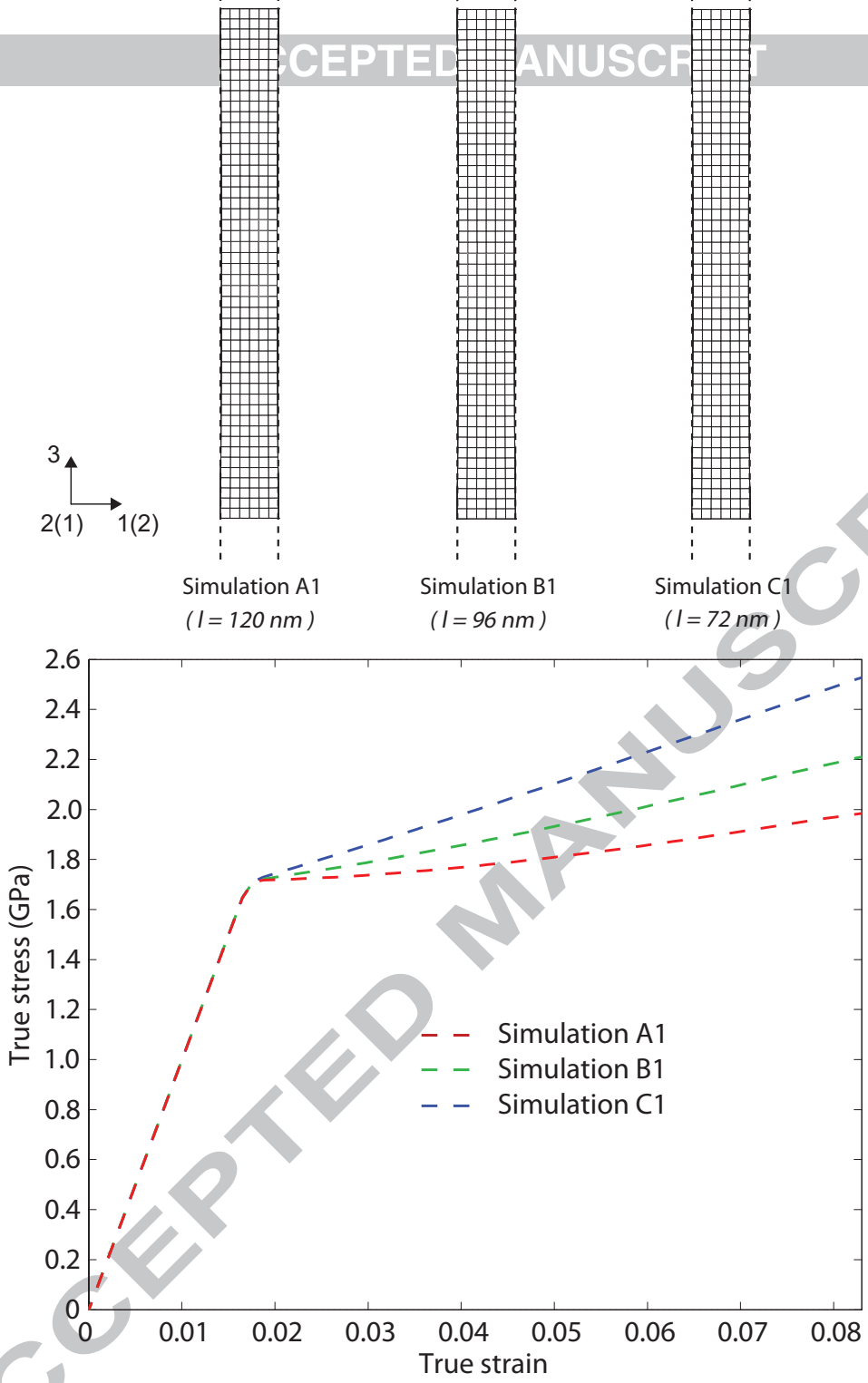

Figure 6: The deformed finite-element mesh of the nanotensile specimen's gage section obtained from Simulations A1, B1 and C1 at a true strain of 8.3%. The dashed vertical lines drawn on the finite-element meshes show that the cross sectional area of each gage section along the loading axis i.e. axis-3 can be treated as being uniform. The true stress vs. true strain curve determined from Simulations A1, B1 and C1 are also shown

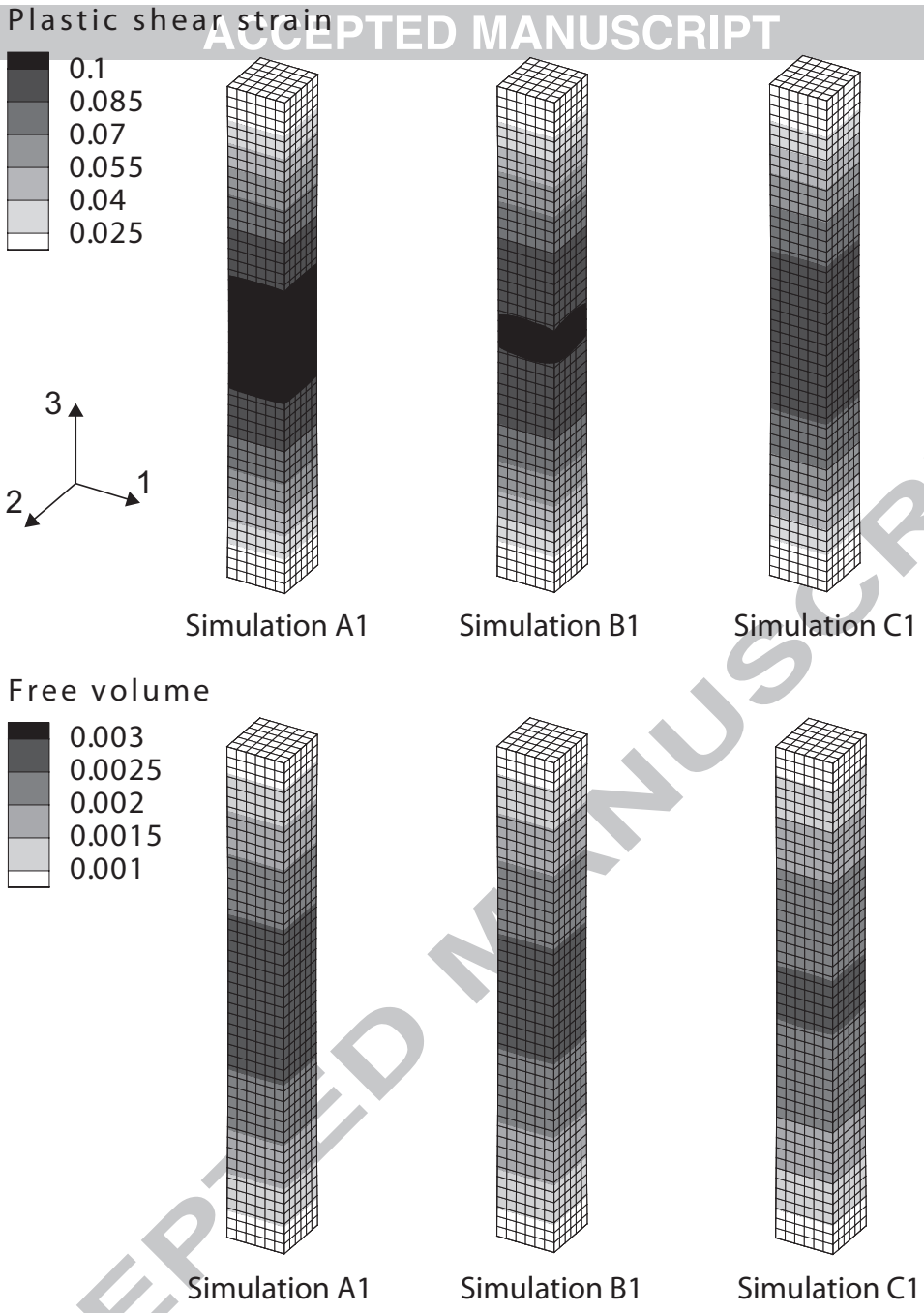

Figure 7: The contour plots of the plastic shear strain and free volume in the nanotensile specimen's gage section modeled in Simulations A1, B1 and C1, determined at a true strain of 5.83%.

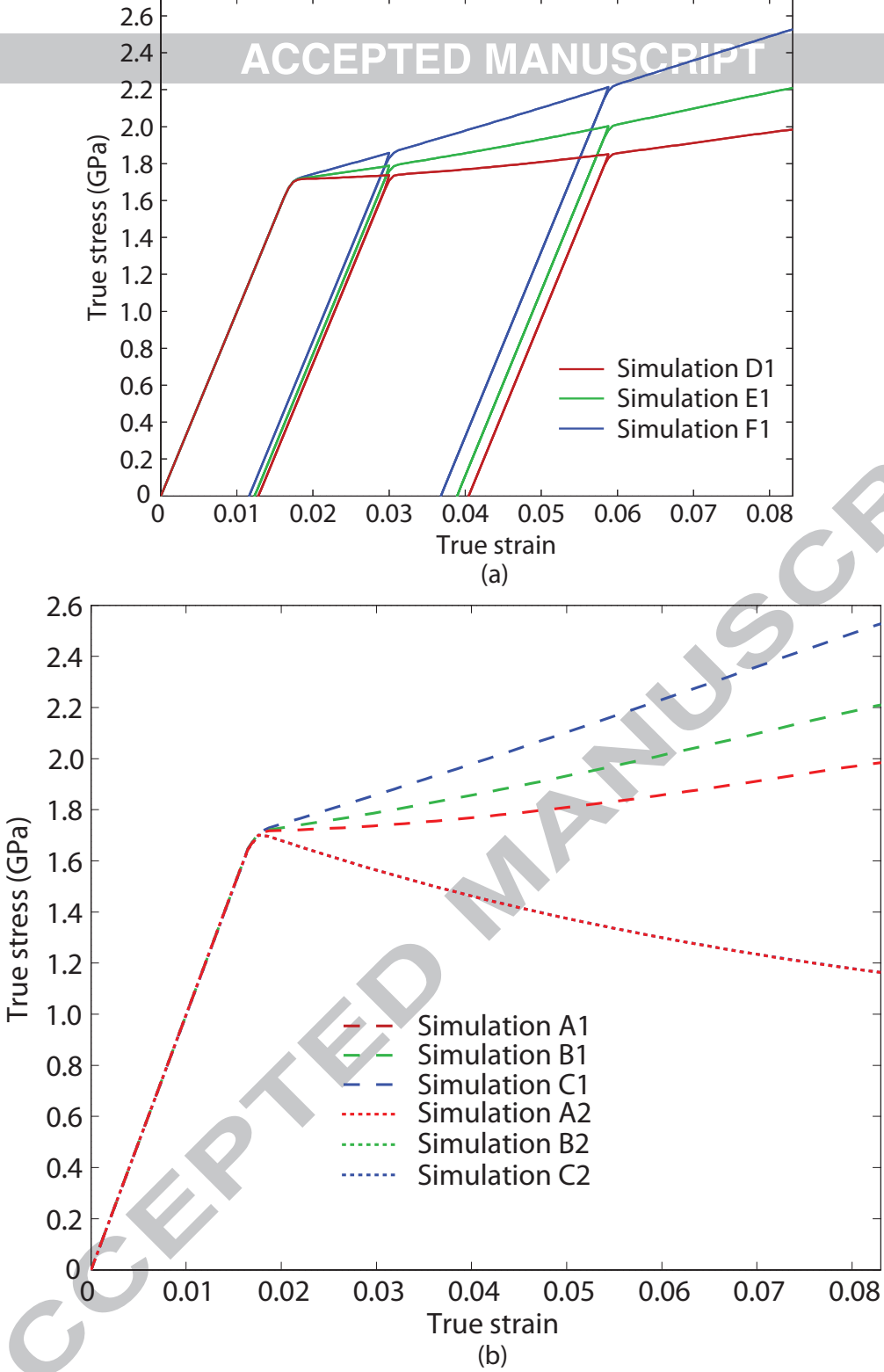

Figure 8: (a) The true stress vs. true strain curve obtained from Simulations D1, E1 and F1. (b) The true stress vs. true strain curve obtained from Simulations A1, B1, C1, A2, B2 and C2. The stress-strain response determined from Simulations A2, B2 and C2 are identical.

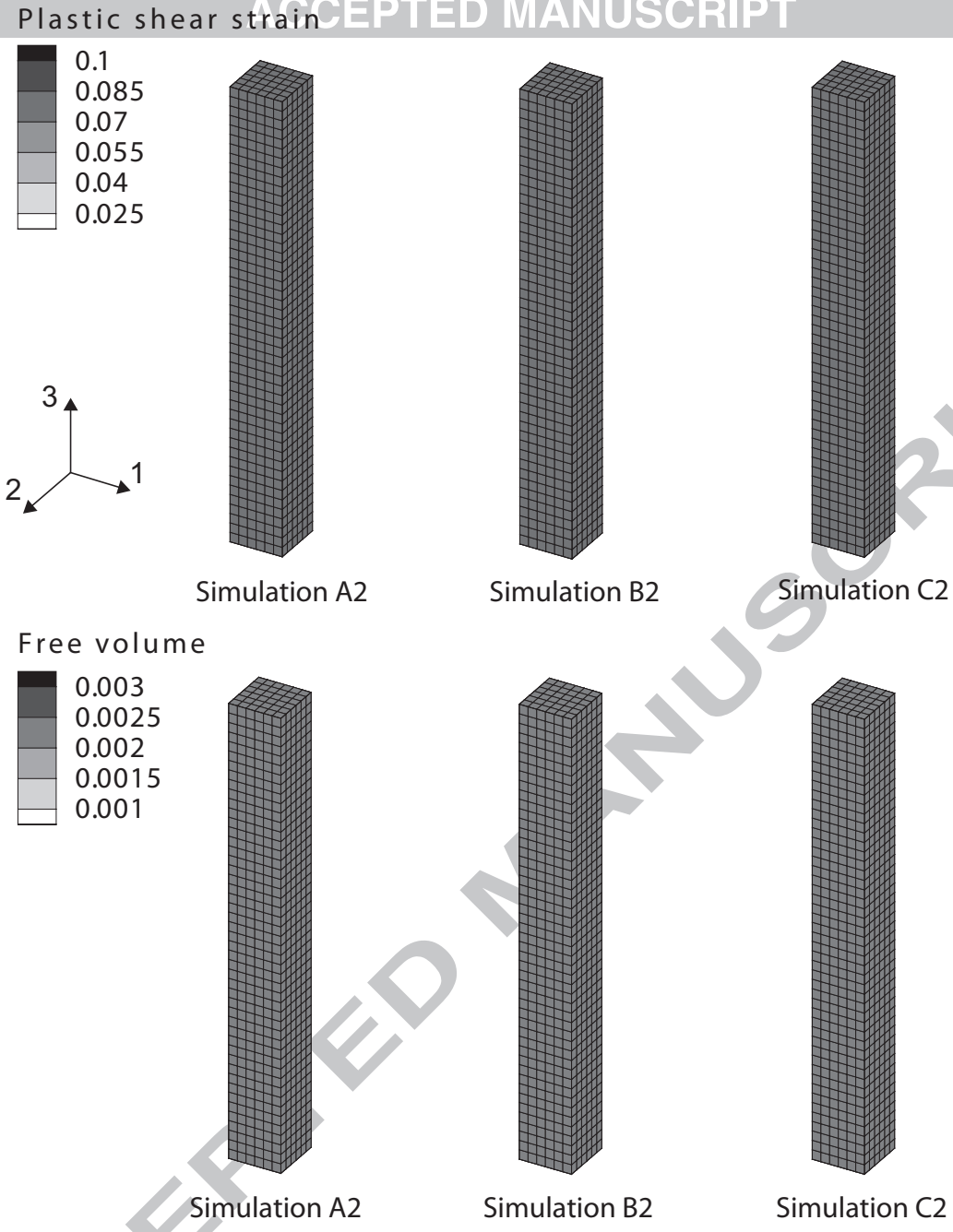

Figure 9: The contour plots of the plastic shear strain and free volume in the nanotensile specimen's gage section modeled in Simulations A2, B2 and C2, determined at a true strain of 5.83%.

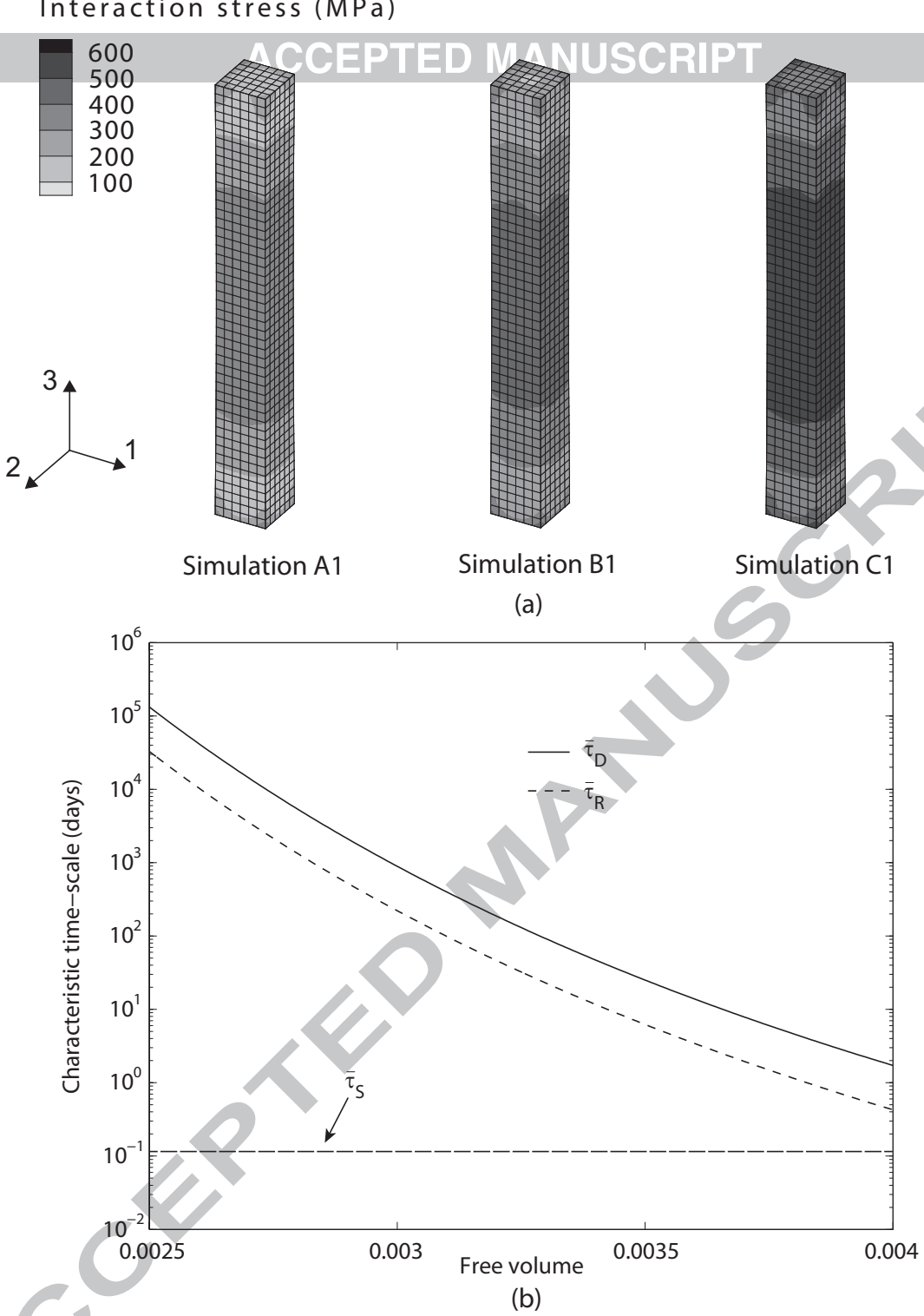

Figure 10: (a) The contour plots of the long-range interaction stress between defects in the nanotensile specimen's gage section modeled in Simulations A1, B1 and C1, determined at a true strain of 5.83%. (b) Variation of the characteristic time-scale for free volume diffusion and relaxation with respect to free volume. The characteristic time-scale for the numerical simulations is also plotted.

Appendix A. Effect of initial free volume distribution on the yield behavior of small-volume metallic glasses

Recently, Zhao et al. (2014) have shown through their simulations that metallic glasses are able to exhibit the "smaller is stronger" or the "smaller is weaker" phenomena depending on the initial conditions for the defects (or free volume) in the sample.

To connect the results from our present theory to the "smaller is stronger" or "smaller is weaker" phenomena in metallic glasses, we must first note that the free volume distribution in amorphous metal samples are inherently heterogeneous (Chen et al., 2011; Li et al., 2013). Prior to sample testing, an initially heterogeneous free volume distribution which is in excess of the thermal equilibrium free volume ξ_T can be induced and "frozen" within an amorphous metal sample at room temperature (due to sluggish free volume diffusion and relaxation kinetics) through non-equilibrium sample processing conditions[13] (Murali and Ramamurty, 2005).

Consider a cylindrical metallic glass bar with an initial diameter d_o and initial length l_o. Let β denote the radial coordinate in the *reference* configuration. For the purpose of the present exercise, we assume for simplicity that the cylindrical sample has a parabolic initial free volume distribution along its radial coordinate i.e.

$$\xi_o = \hat{\xi}_o(\bar{\beta}) = \xi_{mid} - [\xi_{mid} - \xi_{out}]\,\bar{\beta}^2 \tag{A.1}$$

where the normalized radial coordinate, $\bar{\beta} = 2\beta/d_o$. The constants $\xi_{mid} > 0$ and $\xi_{out} > 0$ denote the sample processing-induced initial free volume at the center of the sample and the outer surface of the sample, respectively. We restrict our analysis to low-homologous temperature behavior where the effects of free volume diffusion and structural relaxation can be neglected, and the plastic response is rate-independent. Furthermore, the generation of free volume due to the application of hydrostatic pressure is also neglected in our simplified analysis. Therefore, at *yield point*, the free volume distribution in the bar will be identical to the initial free volume distribution given by equation (A.1) i.e. at yield point, the free volume $\xi = \xi_o$.

[13] Although the Zr-based Vitreloy 1 metallic glass has a thermal equilibrium free volume of 0.06% at room temperature (Yang et al., 2006), experimental measurements have shown that "frozen" free volume as high as 0.5% and 1% have been observed in multi-component Zr-based metallic glasses and an NiP amorphous alloy, respectively (Li et al., 2007).

For the cylindrical sample experiencing plastic deformation under uniaxial tension and assuming $\det \mathbf{F} \approx 1$, the yield function given by equation (16) reduces to

$$T_a \approx \frac{3\sqrt{3}}{3+\zeta}\left(-\zeta\Gamma l_c\left\{\frac{\partial^2\xi}{\partial\beta^2}+\frac{1}{\beta}\frac{\partial\xi}{\partial\beta}\right\}+\zeta s_{\xi 2}(\xi-\xi_T)+c\right) \tag{A.2}$$

where $T_a > 0$ represents the uniaxial tensile stress. We also assume that the initial cohesion, $c_o = \hat{c}_o(\bar{\beta})$. Since $\xi = \xi_o$ and $c = c_o$ at yield point, we then substitute equation (A.1) into equation (A.2), and define the *yield strength*, Y for a given sample as

$$Y \approx \frac{3\sqrt{3}}{3+\zeta}\left\{24\,\zeta\Gamma l_c[\xi_{mid}-\xi_{out}]d_o^{-2}+\min_{0\le\bar{\beta}\le 1}[\zeta s_{\xi_2}(\xi_o-\xi_T)+c_o]\right\}. \tag{A.3}$$

For bulk samples i.e. as $d_o \to \infty$, we obtain

$$Y_\infty \approx \frac{3\sqrt{3}}{3+\zeta}\left\{\min_{0\le\bar{\beta}\le 1}[\zeta s_{\xi_2}(\xi_o-\xi_T)+c_o]\right\} \tag{A.4}$$

from equation (A.3) where Y_∞ represents the yield strength of a bulk sample. Subtracting equation (A.4) from equation (A.3) results in

$$Y - Y_\infty = \frac{72\sqrt{3}}{3+\zeta}\left\{\zeta\Gamma l_c[\xi_{mid}-\xi_{out}]\right\} d_o^{-2}. \tag{A.5}$$

From equation (A.5), we can clearly see that: (a) if $\xi_{mid} > \xi_{out}$, small-volume samples have *higher* yield strengths compared to its bulk counterpart i.e. the "smaller is stronger" phenomenon is obtained, and (b) if $\xi_{mid} < \xi_{out}$, small-volume samples have *lower* yield strengths compared to its bulk counterpart i.e. the "smaller is weaker" phenomenon is obtained.

Before making a *quantitative* comparison of our analytical solution to the nanotensile experiments of Wang et al. (2012) which exhibit the "smaller is stronger" phenomenon, we briefly describe the experiments conducted by Wang et al. (2012) on Al-based amorphous metal samples: with the bulk yield strength $Y_\infty \approx 1.1$ GPa (Yang et al., 2009), we can see from the experimental data of Wang et al. (2012) plotted in Figure A.11 that the yield strength of small-volume samples are higher than the bulk yield strength. In particular, the yield strength generally increases as the sample diameter is reduced from $d_o \sim 400$nm to $d_o \sim 120$nm. As the sample diameters are reduced from $d_o \sim$

120nm, the yield strength approaches a ceiling of $Y \approx 1.8$ GPa (Wang et al., 2012).

To make our quantitative comparison, we choose $\Gamma = 2\text{Jm}^{-2}$ (Zheng and Li, 2009; Zheng and Shen, 2009) and $l_c \approx 600$ μm (Suh et al., 2010). From the orientation of the fracture surface with respect to the loading axis, $\theta \approx 59^o$ (Wang et al., 2012), we can use the relation given in Zhao and Li (2009) to obtain $\zeta \approx 0.45$.

Figure A.11 also shows the comparison of our present model i.e. equation (A.5) with respect to the experimental data of Wang et al. (2012) using $\xi_{mid} - \xi_{out} = 0.07\%$. Despite the numerous simplifications made in our analytical solution, we can see that our theory is able to *quantitatively* fit the variation of the yield strength with respect to sample diameter to reasonable accord[14]. From the results obtained from our present model cf. Figure A.11, we can conclude that very small heterogeneities in the initial free volume distribution within small-volume samples are sufficient to cause significant increases in its yield strength relative to the bulk value.

[14]Since our constitutive theory do not take into account the necessary physics which models the attainment of a yield strength ceiling, we are unable to satisfactorily fit the experimental data for sample diameters $d_o < 120$nm cf. Figure A.11. Within the context of our present theory, we believe that the attainment of a yield strength ceiling could possible stem from the lessening of the initial free volume heterogeneity in samples with diameters $d_o < 120$nm.

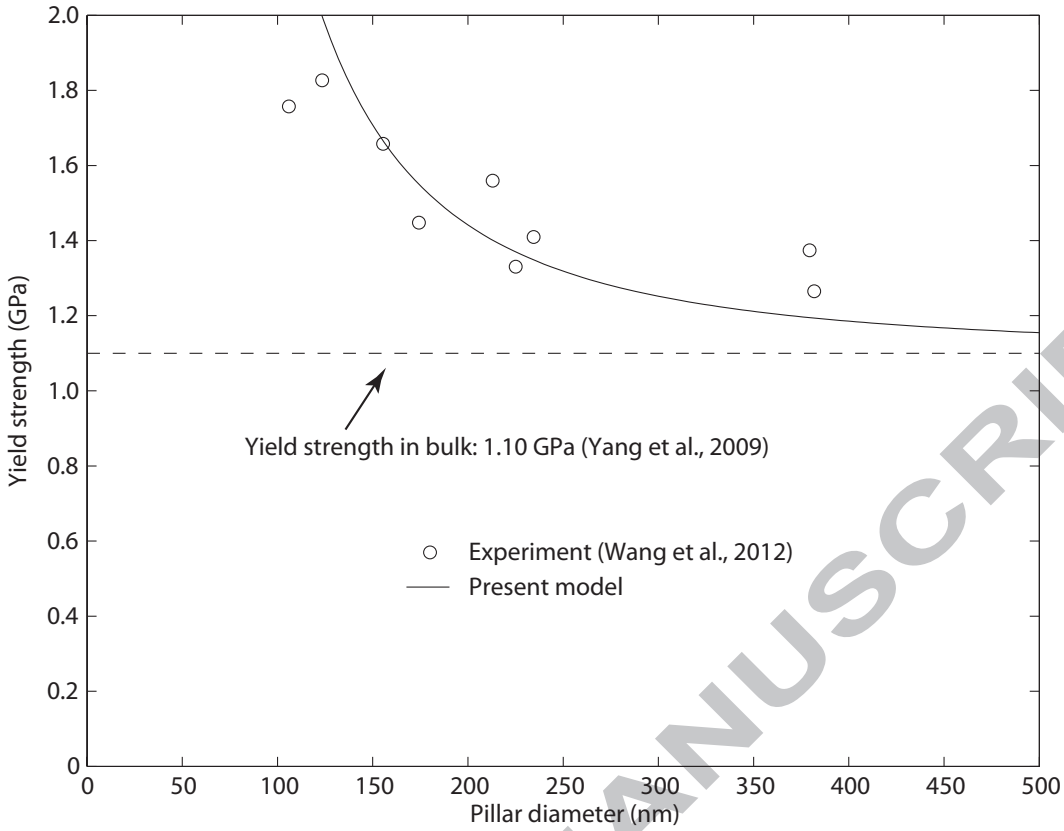

Figure A.11: The fitted yield strength from our analytical calculations i.e. equation (A.5) to the nanotensile experimental data of Wang et al. (2012).

References

Abaqus, 2012. Abaqus Reference Manuals. Simulia Inc. Providence, RI.

Anand, L., Su, C., 2005. A theory for amorphous viscoplastic materials undergoing finite deformations, with application to metallic glasses. J Mech of Phys Solids 53, 1362–1396.

Argon, A., 1979. Plastic deformation in metallic glasses. Acta Metall 27, 47–58.

Bargmann, S., Xiao, T., Klusemann, B., 2014. Computational modelling of submicron-sized metallic glasses. Philos Mag 94, 1–19.

Belytschko, T., Liu, W., Moran, B., 2000. Non-linear finite elements for continua and structures. John Wiley & Sons, New York.

Bharathula, A., Lee, S., Wright, W., Flores, K., 2010. Compression testing of metallic glass at small length scales: Effects of deformation and stability. Acta Mater 58, 5789–5796.

Bittencourt, E., 2014. Dynamic explicit solution for higher-order crystal plasticity theories. Int J Plasticity 53, 1–16.

Bittencourt, E., Needleman, A., van der Giessen, E., Gurtin, M., 2003. A comparison of nonlocal continuum and discrete dislocation plasticity predictions. J Mech Phys Solids 51, 281–310.

Chen, M., 2011. A brief overview of bulk metallic glasses. NPG Asia Mater 3, 82–90.

Chen, Y., Jiang, M., Dai, L., 2011. How does the initial free volume distribution affect shear band formation in metallic glasses? Sci China Phys Mech Astron 54, 1488–1494.

Das, J., Tang, M., Kim, K., Theissmann, R., Baier, F., Wang, W., Eckert, J., 2005. "work-hardenable" ductile bulk metallic glass. Phys Rev Lett 94, 205501.

Dubach, A., Raghavan, R., Loffler, J., Michler, J., Ramamurty, U., 2009. Micropillar compression studies on a bulk metallic glass in different structural states. Scripta Mater 60, 567–570.

Ekambaram, R., Thamburaja, P., Nikabdullah, N., 2008. On the evolution of free volume during the deformation of metallic glasses at high homologous temperatures. Mech Mater 40, 487–506.

Ekambaram, R., Thamburaja, P., Yang, H., Li, Y., Nikabdullah, N., 2010. The multi-axial deformation behavior of bulk-metallic glasses at high homologous temperatures. Int J Solids Struct 47, 678–690.

Guo, H., Yan, P., Wang, Y., Tan, J., Zhang, Z., Sui, M., Ma, E., 2007. Tensile ductility and necking of metallic glass. Nat Mater 6, 734–739.

Gurtin, M., 2002. A gradient theory of single-crystal viscoplasticity that accounts for geometrically necessary dislocations. J Mech Phys Solids 50, 5–32.

Gurtin, M., Anand, L., Lele, S., 2007. Gradient single-crystal plasticity with free energy dependent on dislocation densities. J Mech Phys Solids 55, 1853–1878.

Homer, E., Schuh, C., 2010. Three-dimensional shear transformation zone dynamics model for amorphous metals. Modelling Simul Mater Sci Eng 18, 065009.

Jang, D., Greer, J., 2010. Transition from a strong-yet-brittle to a stronger-and-ductile state by size reduction of metallic glasses. Nat Mater 9, 215–219.

Jang, D., Gross, C., Greer, J., 2011. Effects of size on the strength and deformation mechanism in zr-based metallic glasses. Int J Plasticity 27, 858–867.

Kumar, G., Desai, A., Schroers, J., 2011. Bulk metallic glass: the smaller the better. Adv Mater 23, 461–476.

Lee, M., Han, C., 2010. An explicit approach for strain gradient plasticity formulations. AIP Conf Proc 1252, 935.

Lee, M., Han, C., 2012. An explicit finite element approach with patch projection technique for strain gradient plasticity formulations. Comput Mech 49, 171–183.

Li, G., Liu, J., Liu, R., 2007. Compression behavior of bulk metallic glasses and binary amorphous alloy. Chinese Phys Lett 24, 2323–2326.

Li, J., Spaepen, F., Hufnagel, T., 2002. Nanometre-scale defects in shear bands in a metallic glass. Philos Mag A 82, 2623–2630.

Li, L., Homer, E., Schuh, C., 2013. Shear transformation zone dynamics model for metallic glasses incorporating free volume as a state variable. Acta Mater 61, 3347–3359.

Li, Q., Li, M., 2006. Molecular dynamics simulation of intrinsic and extrinsic mechanical properties of amorphous metals. Intermetallics 14, 1005–1010.

Lu, J., 2002. Mechanical behavior of a bulk metallic glass and its composite over a wide range of strain rates and temperatures. PhD Thesis, California Institute of Technology .

Moran, B., Ortiz, M., Shih, F., 1990. Formulation of implicit finite element methods for multiplicative finite deformation plasticity. Int J Numer Meth Eng 29, 483–514.

Murali, P., Ramamurty, U., 2005. Embrittlement of a bulk metallic glass due to sub-t_g annealing. Acta Mater 53, 1467–1478.

Niordson, C., Legarth, B., 2010. Strain gradient effects on cyclic plasticity. J Mech Phys Solids 58, 542–557.

Pang, J., Tan, M., Liew, K., 2010. Computational study of tensile deformation of a constrained nanoscale metallic glass. Int J Mod Phys B 24, 305–310.

Park, M., Suh, Y., Song, S., 2012. On an implementation of the strain gradient plasticity with linear finite elements and reduced integration. Finite Elem Anal Des 59, 35–43.

Schroers, J., Johnson, W., 2004. Ductile bulk metallic glass. Phys Rev Lett 93, 255506.

Schuh, C., Hufnagel, T., Ramamurty, U., 2007. Mechanical behavior of amorphous alloys. Acta Materialia 55, 4067–4109.

Shi, Y., Falk, M., 2006. Atomic-scale simulations of strain localization in three-dimensional model amorphous solids. Phys Rev B 73, 214201.

Shimizu, F., Ogata, S., Li, J., 2006. Theory of shear banding in metallic glasses and molecular dynamics calculations. Mater T JIM 48, 2923–2927.

Simo, J., Taylor, R., Pister, K., 1985. Variational and projection methods for the volume constraint in finite deformation elasto-plasticity. Comput Meth Appl Mech Eng 51, 177–208.

Spaepen, F., 1977. A microscopic mechanism for steady state inhomogeneous flow in metallic glasses. Acta Metall Mater 25, 407–415.

Suh, J., Conner, R., Kim, C., Demetriou, M., Johnson, W., 2010. Correlation between fracture surface morphology and toughness in zr-based bulk metallic glasses. J Mater Res 25, 320–329.

Thamburaja, P., 2011. Length scale effects on the shear localization process in metallic glasses: A theoretical and computational study. J Mech Phys Solids 59, 1552–1575.

Tian, L., Cheng, Y., Shan, Z., Li, J., Wang, C., Han, X., Sun, J., Ma, E., 2012. Approaching the ideal elastic limit of metallic glasses. Nat Commun 3, 609.

Volkert, C., Donohue, A., Spaepen, F., 2008. Effect of sample size on deformation in amorphous metals. J Appl Phys 103, 083539.

Wang, C., Ding, J., Cheng, Y., Wan, J., Tian, L., Sun, J., Shan, Z., Li, J., Ma, E., 2012. Sample size matters for $al_{88}fe_7gd_5$ metallic glass: Smaller is stronger. Acta Mater 60, 5370–5379.

Yang, B., Morrison, M., Liaw, P., Buchanan, R., Wang, G., Liu, C., Denda, M., 2005. Dynamic evolution of nanoscale shear bands in a bulk-metallic glass. Appl Phys Lett 86, 141904.

Yang, B., Yao, J., Zhang, J., Yang, H., Wang, J., Ma, E., 2009. Al-rich bulk metallic glasses with plasticity and ultrahigh specific strength. Scripta Mater 61, 423–426.

Yang, Q., Mota, A., Ortiz, M., 2006. A finite-deformation constitutive model of bulk metallic glass plasticity. Comput Mech 37, 194–204.

Zhao, M., Li, M., 2009. A constitutive theory and modeling on deviation of shear band inclination angles in bulk metallic glasses. J Mater Res 24, 2688–2696.

Zhao, P., Li, J., Wang, Z., 2014. Extended defects, ideal strength and actual strengths of finite-sized metallic glasses. Acta Mater 73, 149–166.

Zheng, G., Li, M., 2009. Mesoscopic theory of shear banding and crack propagation in metallic glasses. Phys Rev B 80, 104201.

Zheng, G., Shen, Y., 2009. Simulation of crack propagation in fiber-reinforced bulk metallic glass. Int J Solids Struct 47, 320–329.

Zienkiewicz, O., Taylor, R., 2000. The finite element method, Fifth Edition, Volume 1: The basis. Butterworth-Heinemann.